

GPGPU Acceleration of All-Electron Electronic Structure Theory Using Localized Numeric Atom-Centered Basis Functions

William P. Huhn^{a,1}, Björn Lange^{a,2}, Victor Wen-zhe Yu^a, Mina Yoon^b,
Volker Blum^{a,c,*}

^a*Department of Mechanical Engineering and Materials Science, Duke University,
Durham, NC 27708, USA*

^b*Center for Nanophase Materials Sciences, Oak Ridge National Laboratory, Oak Ridge,
TN 37830, USA*

^c*Department of Chemistry, Duke University, Durham, NC 27708, USA*

Abstract

We present an implementation of all-electron density-functional theory for massively parallel GPGPU-based platforms, using localized atom-centered basis functions and real-space integration grids. Special attention is paid to domain decomposition of the problem on non-uniform grids, which enables compute- and memory-parallel execution across thousands of nodes for real-space operations, e.g. the update of the electron density, the integration of the real-space Hamiltonian matrix, and calculation of Pulay forces. To assess the performance of our GPGPU implementation, we performed benchmarks on three different architectures using a 103-material test set. We find that operations which rely on dense serial linear algebra show dramatic speedups from GPGPU acceleration: in particular, SCF iterations including force and stress calculations exhibit speedups ranging from 4.5 to 6.6. For the architectures and problem types investigated here, this translates to an expected overall speedup between 3-4 for the entire calculation (including non-GPU

*Corresponding author

Email address: volker.blum@duke.edu (Volker Blum)

¹Present address: Argonne Leadership Computing Facility, Argonne National Laboratory, Argonne, IL 60439, USA

²Present address: DACS Laboratories GmbH, Erkrath, Nordrhein-Westfalen 40699, Germany

accelerated parts), for problems featuring several tens to hundreds of atoms. Additional calculations for a 375-atom Bi_2Se_3 bilayer show that the present GPGPU strategy scales for large-scale distributed-parallel simulations.

Keywords: GPU Acceleration, High Performance Computing, Electronic Structure, Density Functional Theory, Localized Basis Sets, Domain Decomposition

1. Introduction

Kohn-Sham density-functional theory (KS-DFT) [1, 2] is the primary tool for computational materials prediction across a wide range of areas in science and engineering [3, 4, 5, 6]. One class of KS-DFT codes uses spatially localized atom-centered basis sets, e.g. Gaussian orbitals [7, 8, 9, 10, 11, 12, 13, 14, 15, 16, 17], Slater orbitals [18, 19, 20], and numeric atom-centered orbitals (NAOs). [21, 22, 23, 24, 25, 26, 27, 19, 28, 29, 30, 31] For these basis sets, local operations such as Hamiltonian and overlap matrix integrations, updates of the electron density and its gradients, or parts of force and stress tensor computations, can be carried out on real-space grids. Due to the locality of the basis functions and of the Kohn-Sham potential, these operations can be implemented such that the computational timings scale linearly in number of atoms. [32, 33, 34, 35, 19, 28, 36, 37] Accordingly, in the system size range for which real-space operations dominate the cost – typically small-to-mid-sized calculations comprising several tens to hundreds of atoms – this translates into approximately linear-scaling overall execution times as well. For larger-scale calculations, most KS-DFT codes have a formal default $O(N_{atoms}^3)$ scaling due to the reliance on eigenvalue solvers to directly solve the Kohn-Sham eigenvalue problem for all occupied electron states, known as the “cubic wall” of standard KS-DFT. However, much of the practical science addressed by KS-DFT occurs below this limiting regime and instead in the range where operations with lower scaling exponents still account for the majority of the cost.

An increasingly available paradigm in high-performance computing (HPC) are general purpose graphics processing unit (GPGPU)-accelerated architectures, in which each computational node contains one or more GPGPU accelerators working in tandem with the traditional CPUs employed in HPC applications. GPGPUs are well suited for evaluation of highly vectorizable, compute-intensive algorithms due to their unique massively-parallel

design, prompting early work to demonstrate matrix multiplications [38] and FFTs [39] on commodity hardware. The feasibility of GPU-accelerated electronic structure calculations was demonstrated in works by Ufimtsev and Martínez [40, 41, 42, 43] which would form the basis for the TeraChem electronic structure package [44], as well as by Yasuda using the Gaussian package [45, 46]. Since then, a number of electronic structure packages have incorporated GPU acceleration, including ABINIT [47], ADF [48], BigDFT [49, 50], CP2K [51], GPAW [52, 53, 54], LS3DF [55], octopus [56, 57, 58], ONETEP [59], PETot (now PWmat) [60, 61, 62, 63], Q-Chem [64, 65, 15], Quantum ESPRESSO [66, 67], RMG [68, 69], VASP [70, 71, 72, 73], and FHI-aims (this work). Development cost can be alleviated by using drop-in GPU-accelerated libraries such as cuBLAS [74], cuFFT [75], Thrust [76], ELPA [77, 78, 79], and MAGMA [80, 81, 82] for general mathematical operations. Nevertheless, GPU acceleration is generally not a trivial task due to the need to target low-level algorithms, which constitute the majority of the computational workload, specific to a given software package and port them to a new architecture. However, the raw computational output afforded by GPGPUs can be immense.

In this paper, we describe a careful GPGPU adaption and analysis of several of the dominant real-space operations for KS-DFT in the NAO-based full-potential, all-electron electronic structure code FHI-aims. [30, 37, 83] FHI-aims is a general-purpose electronic structure simulation code, offering proven scalability to thousands of atoms and on very large, conventional distributed-parallel high-performance computers. [84, 77, 85, 86] The code achieves benchmark-quality accuracy for semi-local [87, 17], hybrid [88, 89, 17], and many-body perturbative [88, 90] levels of theory. The specific implementation described here helps unlock the potential of GPGPU architectures for a broad range of production simulations using semilocal DFT, including generalized gradient approximation (GGA) and meta-GGA exchange-correlation functionals. We specifically target Hamilton and overlap matrix integrations, updates of the density and its gradients, and the computation of forces and stress tensor components.

In FHI-aims, linear scaling in the real-space operations covered in this paper is achieved using a real-space domain decomposition (RSDD) algorithm [37], wherein the set of all real-space integration points is subdivided into compact sets of points known as “batches”. As shown below, this RSDD algorithm is naturally parallel in both memory and workload and thus allows for an efficient load-balanced, distributed-parallel GPGPU-assisted im-

plementation. The problem sizes for each individual batch of points are naturally suited for GPGPU acceleration, allowing for the usage of drop-in GPGPU-accelerated libraries with minimal code restructuring necessary for the Hamiltonian matrix integrals, update of density and density gradients, and total energy gradients. The electrostatic potential calculation uses a multipole summation algorithm differing from the RSDD algorithm presented here and thus was not GPGPU-accelerated for this work. Likewise, the exact-exchange operator of hybrid DFT and eigenvalue solutions that can be accessed through libraries such as ELPA [77, 78, 79] and MAGMA [80, 81, 82] are not targeted by this work.

This paper is organized as follows. First, we outline the fundamental equations entering into real-space Kohn-Sham density functional theory. Next, we discuss design principles for numerical algorithms which facilitate optimal usage of GPGPU resources, the RSDD algorithms used for evaluating integrals with FHI-aims and their adaption for execution on GPGPU resources. Finally, timing and scaling benchmarks for four different GPGPU-accelerated architectures and two sets of materials demonstrate GPGPU speedups for real-space integrations across a broad class of architectures and systems encountered in electronic structure based materials simulations.

2. Background

Within the Born-Oppenheimer approximation, the objective of KS-DFT is to determine the electron density $n(\mathbf{r})$ for a given set of fixed nuclear position $\{\mathbf{R}_{at}\}$ of each atom (the “system geometry”). The ground-state total energy $E_{tot}[n]$ and other observables are then evaluated as functionals of $n(\mathbf{r})$. Throughout this section, we assume a non-spin-polarized system for simplicity. However, the extension to collinearly spin-polarized systems is straightforward, as is the extension to spin-orbit coupled and/or non-collinear spin systems, [91] since the underlying matrix integrals, density and gradient updates follow exactly analogous formulae. The density is determined by solving an effective single-particle Hamiltonian \hat{h}_{KS} . In scalar-relativistic form,

$$\hat{h}_{KS} = \hat{t}_s + \hat{v}_{ext} + \hat{v}_H[n] + \hat{v}_{xc}[n] \quad (1)$$

where \hat{t}_s is the (scalar-relativistic) kinetic energy, \hat{v}_{ext} is the external potential, $\hat{v}_H[n]$ is the Hartree potential of the electrons, and $\hat{v}_{xc}[n]$ is the

exchange-correlation potential. Evidently, the density $n(\mathbf{r})$ depends on the Hamiltonian \hat{h}_{KS} and the Hamiltonian depends on the density. Finding a stationary density that yields the particular Hamiltonian that generates this density is a non-linear optimization problem and is cast as a “self-consistent field” (SCF) cycle.

The complete flow of a typical electronic structure calculation is shown in Figure 1, which also indicates the specific operations that are GPU-accelerated in this work. For a given set of initial nuclear positions, the eigenfunctions $\{\psi_l\}$ (with eigenvalues ϵ_l) and/or the stationary density of the Hamiltonian in Eq. (1) are expressed in terms of a finite set of basis functions $\{\varphi_i\}$. For a non-periodic system, this expansion has the form

$$\psi_l(\mathbf{r}) = \sum_{i=1}^{N_b} c_{il} \varphi_i(\mathbf{r}). \quad (2)$$

N_b is the size of the basis set and c_{il} is the coefficient of the l^{th} eigenvector for the i^{th} basis function. The density can then be computed as

$$n(\mathbf{r}) = \sum_{ij} \varphi_i^*(\mathbf{r}) n_{ij} \varphi_j(\mathbf{r}), \quad (3)$$

where n_{ij} is the density matrix, defined as

$$n_{ij} = \sum_l f_l c_{il}^* c_{jl}, \quad (4)$$

where f_l is the occupation number of orbital ψ_l . If n_{ij} is already known, Eq. (4) may be implemented in an $O(N)$ approach for localized basis elements.

Initial guesses for the electronic structure (Figure 1) can either be given in terms of $\psi_l(\mathbf{r})$ or in terms of n_{ij} . In FHI-aims, these initial quantities are produced by solving the Hamiltonian in Eq. (1) for the potential of a sum of overlapping free-atom densities. The density gradient ∇n is required for GGA calculations, where the Hessian $\nabla^2 n$ dependence in the exchange-correlation potential energy may be converted to a ∇n dependence via integration by parts (Eq. (30) of [30]) The Hessian is required for any force computation, or when evaluation of the explicit Kohn-Sham potential for GGAs is needed for any other reason.

In this work, we use localized atom-centered basis functions, which are generally non-orthonormal to one another and yield a non-trivial overlap

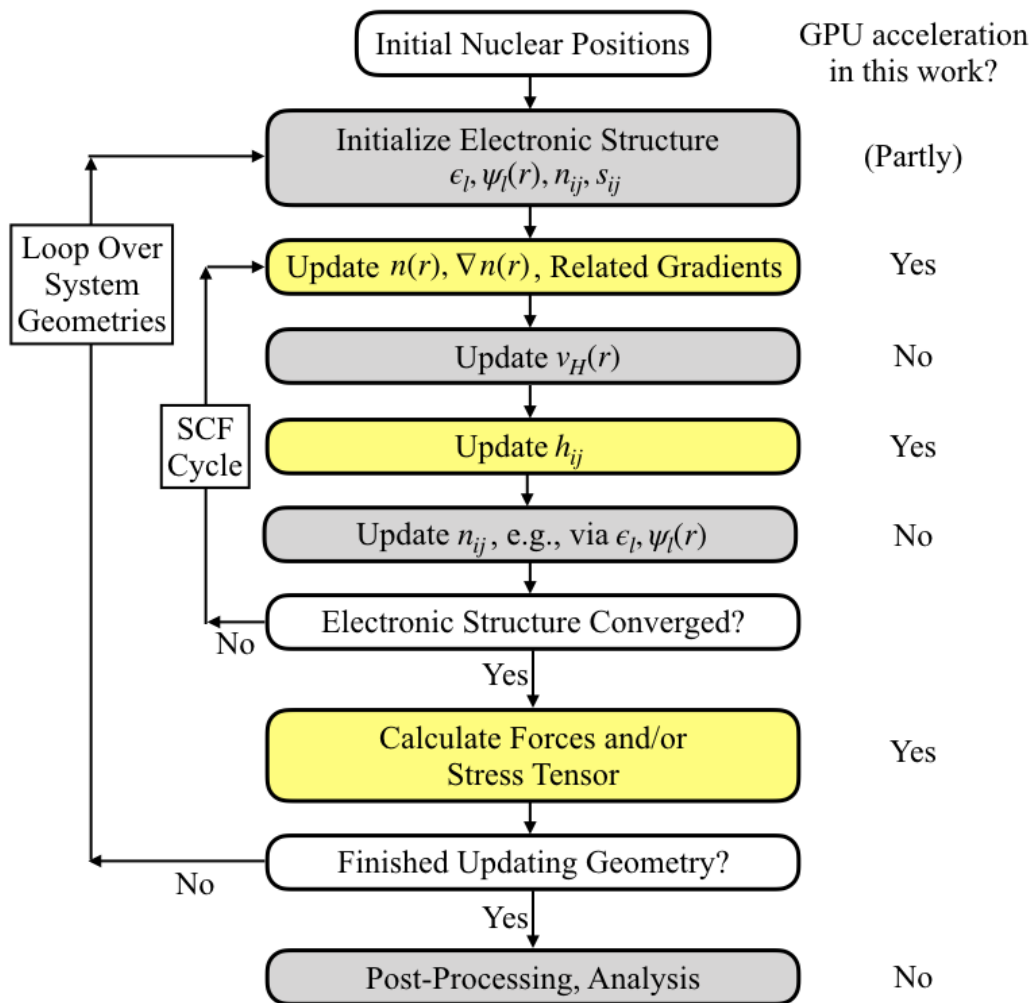


Figure 1: Program flow for a typical electronic structure calculation involving geometry relaxation or molecular dynamics. Shaded boxes indicate steps contributing to the actual computational workload. Yellow shading indicates steps that are subject to real-space GPU acceleration in this work, whereas gray shading indicates steps that are GPU-accelerated only partly, not at all, or that are handled by separate software components [92, 77, 79, 78, 86] outside the scope of this work.

matrix

$$s_{ij} = \int d\mathbf{r} [\varphi_i(\mathbf{r})\varphi_j(\mathbf{r})]. \quad (5)$$

For periodic systems, we discretize the eigenvectors in terms of Bloch orbitals $\{\chi_{i\mathbf{k}}\}$ that are extended throughout the entire crystal:

$$\psi_{l\mathbf{k}}(\mathbf{r}) = \sum_{i=1}^{N_b} c_{il}(\mathbf{k})\chi_{i\mathbf{k}}(\mathbf{r}). \quad (6)$$

\mathbf{k} is the crystal momentum quantum number and N_b is the number of basis functions associated with a single unit cell. Each $\chi_{i\mathbf{k}}$ is associated with a particular localized basis function $\varphi_i(\mathbf{r})$ and its periodic images in all other unit cells (labelled by lattice translation vectors \mathbf{T}) via the transformation

$$\chi_{i\mathbf{k}}(\mathbf{r}) = \sum_{\mathbf{T}} e^{i\mathbf{k}\cdot\mathbf{T}} \varphi_i(\mathbf{r} - \mathbf{T}). \quad (7)$$

As a result, $\chi_{i\mathbf{k}}(\mathbf{r})$ is normalized per unit cell. The relevant overlap matrix is then

$$s_{ij}(\mathbf{k}) = \int_{\text{unit cell}} d\mathbf{r} [\chi_{i\mathbf{k}}^*(\mathbf{r})\chi_{j\mathbf{k}}(\mathbf{r})]. \quad (8)$$

Importantly, for spatially localized real-space basis functions $\{\varphi_i(\mathbf{r})\}$, and using Eqs. (6) and (7), the density matrix can also be expressed in terms of the real-space basis functions, just like in Eq. (3). The difference is that the sum in Eq. (3) now runs over real-space basis functions and their images both inside and outside a given unit cell. More precisely, since only grid points \mathbf{r} inside a single cell (say, the cell at $\mathbf{T}=(0,0,0)$) need be considered, i and j in Eq. (3) run from 1, ..., N_{rs} , where N_{rs} is the number of all localized real-space basis functions in the crystal that are non-zero somewhere inside the volume of the unit cell at $\mathbf{T}=(0,0,0)$.

As mentioned above and as indicated in Figure 1, the density computation Eq. (3), which has the form of matrix multiplications, is GPU-accelerated in this work. Additionally, the calculation of density gradients $\nabla n(\mathbf{r})$ is necessary for almost any current density functional approximations, i.e., GGA and beyond. Finally, the Hessian matrix of the density, $\partial_{x_i}\partial_{x_j}n(\mathbf{r})$ ($i, j=1, \dots, 3$), is needed at least for total energy gradient calculations (forces and stresses). For a given density matrix, these gradients are straightforward extensions of Eq. (3), but their evaluation can still contribute significantly to the overall

computational cost: $\nabla n(\mathbf{r})$ has three components, $\partial_{x_i}\partial_{x_j}n(\mathbf{r})$ has six components, and each component has the same cost as the evaluation of $n(\mathbf{r})$ itself.

As a next step, the Hartree potential $\hat{v}_H[n]$ in Eq. (1) is a local operator of the form

$$\hat{v}_H[n](\mathbf{r}) = \int d\mathbf{r}' \frac{n(\mathbf{r}')}{|\mathbf{r} - \mathbf{r}'|}. \quad (9)$$

In practice, \hat{v}_{ext} (which includes the potential due to the nuclei) and $\hat{v}_H[n]$ (the averaged electrostatic potential due to the electron density) are treated together in order to evaluate an overall charge-neutral system. As mentioned above, this full electrostatic potential may be computed via a multipole summation scheme [30] and is not subject to GPGPU acceleration in this work. In the system range investigated here, it does not dominate the computational cost.

In non-periodic system geometries and for real-valued local basis functions $\varphi_i(\mathbf{r})$, the Hamiltonian is naturally expressed in terms of matrix elements h_{ij} with an integral form of

$$h_{ij} = \int d\mathbf{r} [\varphi_i(\mathbf{r}) \hat{h}_{KS} \varphi_j(\mathbf{r})]. \quad (10)$$

In periodic boundary conditions,

$$h_{ij}(\mathbf{k}) = \int_{\text{unit cell}} d\mathbf{r} [\chi_{i\mathbf{k}}^*(\mathbf{r}) \hat{h}_{KS} \chi_{j\mathbf{k}}(\mathbf{r})]. \quad (11)$$

In the periodic case, each matrix element $h_{ij}(\mathbf{k})$ can still be summed up from local real-space integrals (the equivalent of Eq. (10)) of the following type:

$$h_{ij}^{\text{uc}} = \int_{\text{unit cell}} d\mathbf{r} [\varphi_i(\mathbf{r}) \hat{h}_{KS} \varphi_j(\mathbf{r})]. \quad (12)$$

However, in contrast to the non-periodic case, the running indices i and j for h_{ij}^{uc} in Eq. (12) are not restricted to $1, \dots, N_b$ (the number of basis functions associated with a single unit cell) but instead run over $1, \dots, N_{\text{rs}}$, the number of localized real-space basis functions in the crystal that are non-zero somewhere inside the volume of the unit cell at $\mathbf{T}=(0,0,0)$. The local integrals h_{ij}^{uc} can be computed using the exact same real-space integration code as their non-periodic equivalents. The only difference is that each integration point \mathbf{r} is mapped back to its periodic image within the unit cell at $\mathbf{T}=(0,0,0)$, so that

the local integrals in Eq. (12) are restricted to that unit cell. The full Bloch integrals $h_{ij}(\mathbf{k})$ can then be constructed by inserting Eq. (7) into Eq. (11). The expression for $h_{ij}(\mathbf{k})$ becomes a sum over individual real-space integrals of form h_{ij}^{uc} , multiplied by Bloch phase factors $e^{i\mathbf{k}\cdot(\mathbf{T}_i-\mathbf{T}_j)}$ that connect the unit cells where the real-space basis functions i and j are centered. The overlap matrix elements $s_{ij}(\mathbf{k})$ can be constructed analogously. To unify the notation between periodic and non-periodic systems, we will refer to both Eqs. (10) and (12) as the “real-space Hamiltonian matrix” h_{ij}^{uc} for the remainder of this paper. As shown in Figure (1), its computation is GPU-accelerated in this work.

Given the updated KS-DFT Hamiltonian, the Hamiltonian’s approximate eigenvectors $\psi_{l\mathbf{k}}(\mathbf{r})$ and eigenvectors $\epsilon_{l\mathbf{k}}$ can now be found by solving

$$\sum_j h_{ij}(\mathbf{k})c_{jl}(\mathbf{k}) = \epsilon_{l\mathbf{k}} \sum_j s_{ij}(\mathbf{k})c_{jl}(\mathbf{k}) \quad (13)$$

(for non-periodic systems, the \mathbf{k} index may just be omitted). A new density matrix n_{ij} can thus be found. The eigenvector-based approach Eq. (13) scales computationally at least as $O(N_e^3)$, where N_e is the number of electrons in the system. Alternatively, the KS eigenvalue problem may be circumvented entirely by density-matrix-based solvers, [93, 94, 95, 86] often with reduced-dimensional scaling. In FHI-aims, the solution of the KS eigenvalue equation in matrix form is performed via the dense generalized eigensolver library ELPA [92, 77, 79, 78] or circumvented by other solvers interfaced through ELSI [86], an open-source library which provides an interface layer between KS-DFT codes and methods that solve or circumvent the Kohn-Sham eigenvalue problem in density-functional theory. The GPU acceleration or circumvention of Eq. (13) is thus not the topic of this paper; however, options exist in the form of the open-source, GPU-accelerated ELPA and MAGMA eigensolver libraries that are benchmarked elsewhere in the literature. [78, 79, 80, 81, 82]

After the SCF cycle for a given geometry is complete, electronic structure calculations may continue by changing the geometry of a material as the calculation progresses, e.g. to find a local minimum-energy geometry at the Born-Oppenheimer surface, or for molecular dynamics. In these cases, the position of atomic nuclei, \mathbf{R}_{at} , are updated by calculating the forces on each atom,

$$\mathbf{F}_{at} = -\frac{\partial}{\partial \mathbf{R}_{at}} E_{tot}, \quad (14)$$

as a function of the electronic structure after the SCF cycle has converged. Here, E_{tot} is the Born-Oppenheimer total energy of the material and the subscript at labels different atoms for convenience. For localized basis elements, the computationally expensive portion of Eq. (14) is the Pulay forces, which on the scalar-relativistic – here, the atomic zero-order regular approximation (atomic ZORA; cf. Eqs. (55) and (56) in [30]) – and GGA level have the form

$$\mathbf{F}_{at}^P = \mathbf{F}_{at}^{P,local} + \mathbf{F}_{at}^{GGA} + \mathbf{F}_{at}^{at.ZORA} \quad (15)$$

where

$$\begin{aligned} \mathbf{F}_{at}^{P,local} = & -2 \sum_{ij} \int_{\text{unit cell}} d\mathbf{r} [[\nabla_{at}\varphi_i(\mathbf{r})]n_{ij}\hat{h}_{KS}\varphi_j(\mathbf{r})] \\ & + 2 \sum_{ij} \int_{\text{unit cell}} d\mathbf{r} [[\nabla_{at}\varphi_i(\mathbf{r})]q_{ij}\varphi_j(\mathbf{r})], \end{aligned} \quad (16)$$

is the local (density-only) parts of the Pulay forces,

$$q_{ij} = \sum_l f_l \sum_{\mathbf{k}} \epsilon_{lk} c_{il}^*(\mathbf{k}) c_{jl}(\mathbf{k}), \quad (17)$$

is the q_{ij} energy-weighted density matrix,

$$\begin{aligned} \mathbf{F}_{at}^{GGA} = & -4 \sum_{ij} \int d\mathbf{r} [[\nabla_{at}\varphi_i(\mathbf{r})]n_{ij}[\frac{\partial f_{xc}}{\partial |\nabla n|^2} \nabla\varphi_j(\mathbf{r}) \cdot \nabla n(\mathbf{r})]] \\ & -4 \sum_{ij} \int d\mathbf{r} [\varphi_i(\mathbf{r})n_{ij}[\frac{\partial f_{xc}}{\partial |\nabla n|^2} \nabla_{at}\nabla\varphi_j(\mathbf{r}) \cdot \nabla n(\mathbf{r})]] \end{aligned} \quad (18)$$

is the correction to the Pulay forces arising from explicit density gradients in GGA, and

$$\mathbf{F}_{at}^{at.ZORA} = - \sum_{ij} \int d\mathbf{r} [[\nabla_{at}\hat{t}_{at.ZORA}\varphi_i(\mathbf{r})]n_{ij}\varphi_j(\mathbf{r})] \quad (19)$$

is the correction to the Pulay forces arising from atomic ZORA.

For periodic calculations, one may also calculate overall stresses on the computational cell by calculating the stress tensor

$$\sigma_{\lambda\mu} = \frac{1}{V} \left. \frac{\partial E_{tot}}{\partial \epsilon_{\lambda\mu}} \right|_{\epsilon=0} \quad (20)$$

after the SCF cycle has converged. Here, $\epsilon_{\lambda\mu}$ is the symmetric, infinitesimal strain tensor and V is the volume of the computational cell. A full account of the terms that make up the stress tensor in an atom-centered basis set is given in [83].

As mentioned above, the computation of the gradients Eqs. (14) and (20) using atom-centered basis functions for semilocal density functionals can include the numerically expensive evaluation of higher density derivatives such as the density Hessian and similar quantities evaluated on a real-space grid. When needed, the computational cost of Eqs. (14) and (20) can therefore amount to a large fraction of the overall time required to execute the type of computation shown in Figure 1. The corresponding steps are thus also GPU accelerated in this work, using the same real-space grid techniques as for the density and the Hamilton matrices, outlined below.

3. Implementation

3.1. Design Principles for GPGPU-Accelerated Code

There are three major design priorities entering into GPGPU acceleration of an algorithm:

- The workload offloaded to the GPGPU should be highly vectorizable,
- Thread-divergent branching statements (e.g. “if” statements that can lead to different conditional states for different threads) should be avoided in the workload offloaded to the GPGPU, and
- Communication between the CPU and GPGPU over relatively slow buses should be minimized.

Sections of an algorithm which are not easily vectorizable and/or contain a large number of thread-divergent branching statements should be performed by the CPU(s), and sections of an algorithm that are easily vectorizable should be offloaded to the GPGPU. Ideally, GPGPU and CPU workloads should be carried out in parallel in an asynchronous fashion if that is possible. There is an additional design priority implicit in this scheme: the problem size for the workload offloaded to the GPGPU must fit into the GPGPU’s onboard memory.

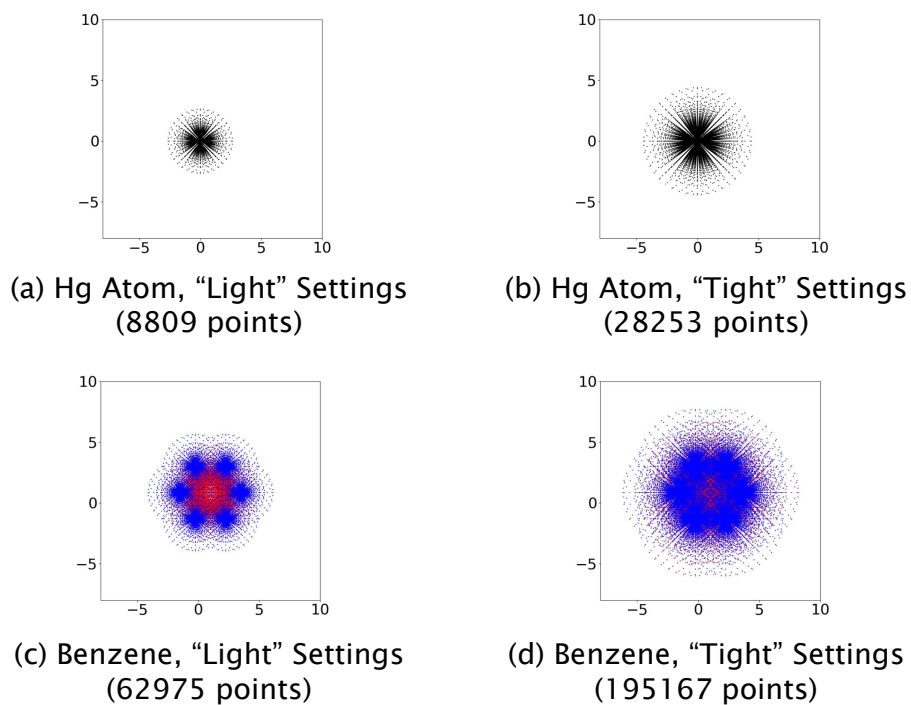


Figure 2: Visualization of real-space integration points for two simple molecules: a mercury atom with (a) "light" and (b) "tight" integration settings and a benzene molecule with (c) "light" and (d) "tight" integration settings. The number of integration points contained in each subfigure is listed in the caption. In subfigures (c) and (d), integration points generated from the carbon and hydrogen atoms are marked red and blue, respectively. Units are in bohr.

3.2. Computational Choices in FHI-aims

3.2.1. Real-Space Integration Grids

A visualization of the real-space integration grids in FHI-aims for a mercury atom is shown in Figures 2a (light settings of FHI-aims) and 2b (tight settings of FHI-aims). Analogous figures for the multi-atom benzene molecule are shown in Figures 2c and 2d. The grid consists of spherical shells of points around each nucleus, with individual grid points located on each shell according to the point distributions described by Lebedev *et al.* [96, 97, 98] and Delley [99]. For the mercury atom, the outermost spherical shells can be observed as “rays” of points far from the respectively nuclei. Closer to the nucleus, there are less points per spherical shell, but the radial density of spherical shells increases systematically (see Eq. 18 in [30]) to account for rapidly varying wavefunctions.

In polyatomic systems like benzene, every atom contributes integration points to the overall integration grid of the system. The radial cutoffs for the radial integration grids well exceed bond lengths in molecules and materials, leading to a densely-interlocking, irregular cloud of integration points covering both nuclear and interstitial regions. Integration weights $w(\mathbf{r})$ are calculated on-the-fly (see Eq. (111) and Appendix C in [83] for the exact definition of the respective weight functions used in FHI-aims), yielding a form for the real-space Hamiltonian integration

$$h_{ij} = \sum_{\mathbf{r}} w(\mathbf{r}) \varphi_i^*(\mathbf{r}) \hat{h}_{KS} \varphi_j(\mathbf{r}) \quad (21)$$

or (for periodic systems)

$$h_{ij}^{uc} = \sum_{\mathbf{r}} w(\mathbf{r}) \varphi_i^*(\mathbf{r}) \hat{h}_{KS} \varphi_j(\mathbf{r}). \quad (22)$$

FHI-aims calculates $w(\mathbf{r})$ using a partition-of-unity approach [100] with a modified form of the $O(N_{atom})$ partitioning scheme proposed by Stratmann *et al.* [33] (see Eqs. 111-112 and C.5-C.8 in Knuth *et al.* [83]), where N_{atom} is the number of atoms in the computational cell. Here, it is sufficient to note that the resulting set of points is not an simple even-spaced grid and may be freely distributed across processes. Also, the process to update overlap matrix integrals s_{ij} or s_{ij}^{uc} (once per SCF cycle) is exactly analogous to the process outlined below for the elements of the Hamiltonian.

The default basis sets $\{\varphi_i(\mathbf{r})\}$ used by FHI-aims for evaluating Eq. (22) are preconstructed sets of numerical atom-centered orbitals (NAO) optimized for KS-DFT-based total energy calculations, as outlined in [30]. The NAO basis sets used in FHI-aims have been shown to have accuracy on par with the best available benchmark codes for total and atomization energies of molecules [17] and calculated equations of state and band energies for solids [87, 91]. A cutoff potential is used to smoothly limit the spacial extent of the basis functions. The cutoff potential (Eq. (9) in [30]) reaches infinity at a user-definable outermost edge that is 6 Å for most chemical species using tight settings. Thus, any radial functions approach zero smoothly at this radius and remain zero at larger distances from their center.

3.3. Real-Space Domain Decomposition (RSDD)

The RSDD is used for the update of the electron density and integration of various matrix elements for semi-local operators. We will focus on integration of the real-space Hamiltonian matrix (Eqs. (10) and (12)) in this section, although the procedure presented applies to matrix elements of an arbitrary semi-local operator. Additional steps related to the electron density update will be presented when relevant. A detailed study of the expected linear scaling in runtime of the RSDD algorithm, including an examination of the performance of various partitioning schemes for integration points, was performed by Havu *et al* [37].

3.3.1. Grid Partitioning

Figure 3a shows a visualization of the partitioning of the set of integration points P into mutually-disjoint “batches” of points $B_\nu \subset P$. Each batch is a compact, spatially-local set of points on which vectorized operations will be performed and are distributed in a round-robin fashion among processes. At no time does any individual process have knowledge of the full real-space integration grid.

The partitioning is accomplished by using a “grid adapted cut-plane method” (Algorithm 3 of [37]) in which the full set P is iteratively divided to smaller subsets using cut-planes (red lines in 3a) until some targeted number of points per subset is reached. The resulting subsets are the batches B_ν . The targeted number of points per batch will be denoted as the “batch size” throughout this paper. The default batch size in FHI-aims is 100 points per batch for CPU-only calculations and 200 points per batch for

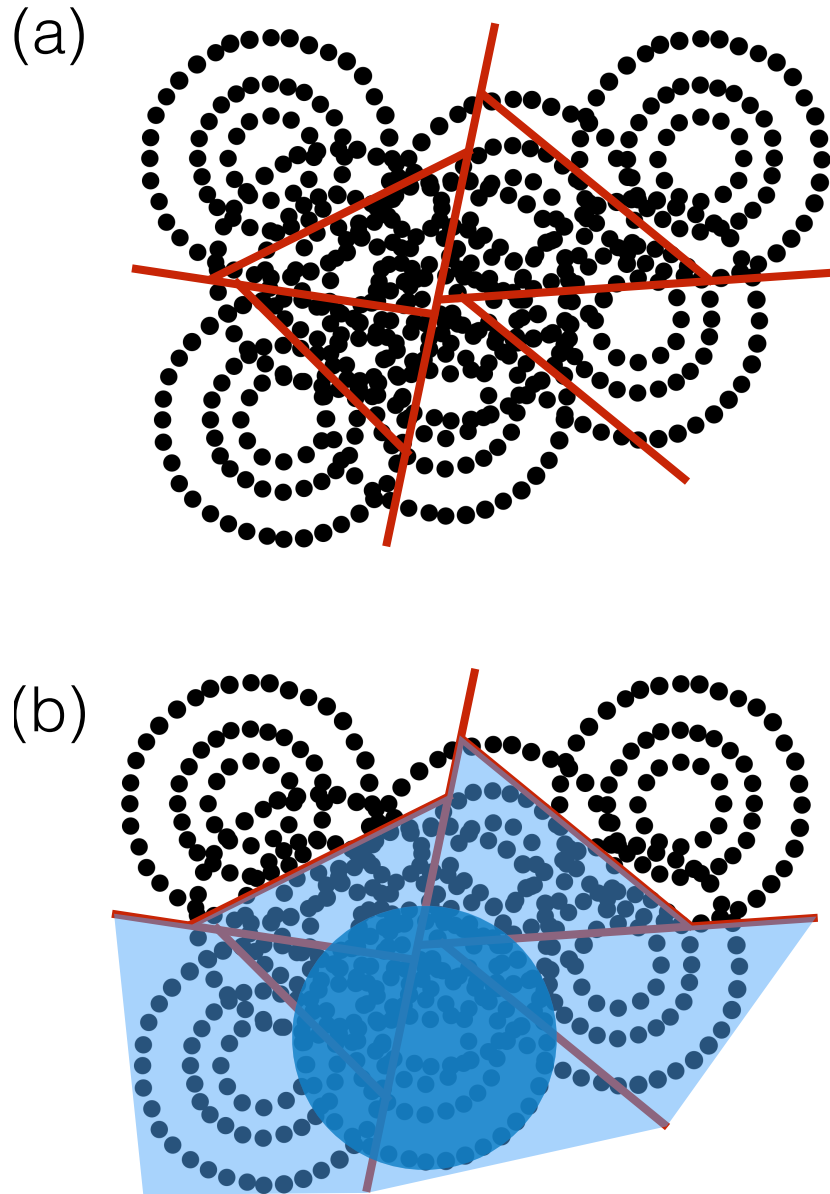


Figure 3: A visualization of the batch partitioning scheme used by FHI-aims. Black points denote integration points, and red lines denote boundaries between batches of points. In subfigure (b), the dark blue circle denotes the support of a local basis function, and batches on which the local basis function has non-zero support are highlighted in light blue.

GPGPU-accelerated calculations. We increase the batch size for GPGPU-accelerated calculations as this will decrease the number of batches, decreasing the amount of CPU-GPU communication and increasing the amount of work accelerated per batch. In our tests, increasing the batch size beyond 200 points does not lead to further overall acceleration.

3.3.2. Parallelization and Dimensionality Reduction

Having generated a set of mutually disjoint batches $\{B_\nu\}$, we may rewrite Eq. (22) as

$$h_{ij}^{uc} = \sum_{\nu} h_{ij}^{uc}[B_\nu] \quad (23)$$

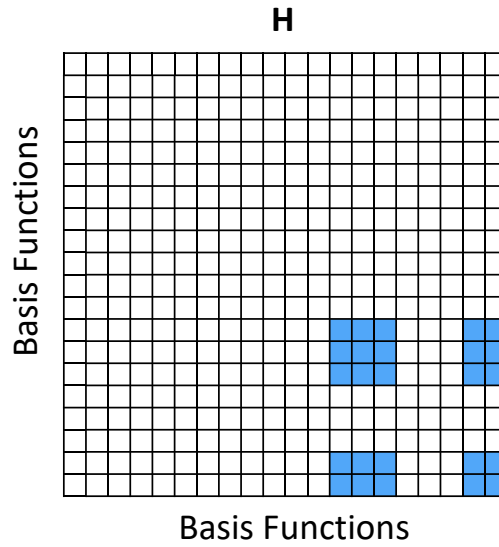
where

$$h_{ij}^{uc}[B_\nu] = \sum_{\mathbf{r} \in B_\nu} w(\mathbf{r}) \varphi_i^*(\mathbf{r}) \hat{h}_{KS} \varphi_j(\mathbf{r}) \quad (24)$$

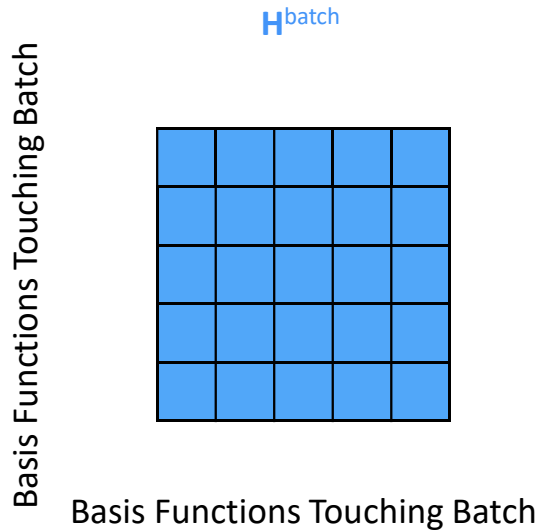
is the contribution of batch B_ν to the real-space Hamiltonian matrix element h_{ij}^{uc} . Eqs. (23) and (24) are trivially parallelizable over batches. The RSDD algorithm parcels out batches to MPI tasks, so that each MPI task owns multiple batches, and each batch is owned uniquely by a single MPI task [37].

The indices in Eqs. (23) and (24) by default run over all basis functions. $h_{ij}^{uc}[B_\nu]$ for a given batch B_ν will be sparse for medium-to-large-sized systems, as many basis functions are centered too far away to touch the integration points in B_ν . While it may be tempting to store $h_{ij}^{uc}[B_\nu]$ in a sparse format, the usage of a sparse matrix format will introduce an intermediate non-trivial indexing step when accessing the matrix elements, impeding vectorization due to indirect addressing. More importantly, the sparse representations for matrices h_{ij}^{uc} and $h_{ij}^{uc}[B_\nu]$ will scale in size as $O(N_{atom})$. Retaining local copies of the full $h_{ij}^{uc}[B_\nu]$ on each separate MPI process will eventually become the dominant memory cost of the calculation.

For each batch, we instead define a reduced-dimensional subspace $\text{nnz}(B_\nu)$ consisting of basis functions with support on the batch, i.e., basis functions that are nonzero on at least part of the grid points in this batch. $h_{ij}^{uc}[B_\nu]$ can be considerably reduced in size by calculating only matrix elements between basis elements φ_i lying in $\text{nnz}(B_\nu)$, yielding a dense ‘‘batch Hamiltonian matrix’’ with form identical to Eq. (24). We take $h_{ij}^{uc}[B_\nu]$ to refer to this subspace batch Hamiltonian matrix for the rest of this paper. When evaluating the electron density update (Eq. (3)) using the RSDD algorithm, an analogous subspace representation is employed for the density matrix $n_{ij}[B_\nu]$ and



(a) Indexing of “Full” Matrix from Batch Matrix



(b) Reduced Dimensionality of Batch Matrix

Figure 4: The contribution of a batch to (a) the real-space Hamiltonian matrix and (b) the batch Hamiltonian matrix. Blue squares indicate matrix elements h_{ij}^{uc} to which the batch may contribute, and white squares denote matrix elements with no contribution from the batch. We show the real-space Hamiltonian matrix as an uncompressed full matrix for simplicity; see Figure 5 for the matrix layouts used in FHI-aims.

(if required) for the energy-weighted density matrix $q_{ij}[B_\nu]$ when calculating Pulay forces (Eq. (14)) and the stress tensor (Eq. (20)).

Defining the $\|\text{nnz}(B_\nu)\| \times \|B_\nu\|$ matrix,

$$K_{ir} \equiv w(\mathbf{r})\varphi_i^*(\mathbf{r}), \quad (25)$$

and the $\|B_\nu\| \times \|\text{nnz}(B_\nu)\|$ matrix

$$L_{rj} \equiv \hat{h}_{KS}\varphi_j(\mathbf{r}), \quad (26)$$

all matrix elements of $h_{ij}^{uc}[B_\nu]$ may be evaluated simultaneously by rewriting Equation 24 as a matrix multiplication

$$h_{ij}^{uc}[B_\nu] = \sum_{\mathbf{r} \in B_\nu} K_{ir} L_{rj}. \quad (27)$$

A visualization of the difference between h_{ij}^{uc} and $h_{ij}^{uc}[B_\nu]$ is provided in Figure 4. h_{ij}^{uc} is a sparse matrix for large systems and localized basis sets, since only a bounded number of basis functions in some proximity to one another will overlap. $h_{ij}^{uc}[B_\nu]$, in contrast, is dense for sufficiently compact set of points, e.g., a sufficiently small batch, since its indices only run over the subset of basis functions that are non-zero anywhere within the compact set of grid points (i.e., these basis functions are already located close to one another). It therefore has a memory consumption of $\|\text{nnz}(B_\nu)\|^2$.

While different batches will have different values for $\|\text{nnz}(B_\nu)\|$ depending on local basis set density and geometry, there exists some upper limit $\max(\|\text{nnz}(B_\nu)\|)$ for the number of basis functions interacting with any batch. $\max(\|\text{nnz}(B_\nu)\|)$ depends on basis set density and local geometry *but not on the system size*. The independence of the size of each batch from the overall system size is responsible for the observed $O(N_{atom})$ execution of integrals, as shown in Havu *et al.* [37].

Once $h_{ij}^{uc}[B_\nu]$ has been calculated, the local copy of h_{ij}^{uc} on each MPI task (here denoted $h_{ij}^{uc,task}$) is updated. There are two matrix formats for the local copy of h_{ij}^{uc} commonly used in FHI-aims: a globally-indexed compressed sparse row (CSR) format and a locally-indexed dense format. Both are further explained in two subsections below. The term ‘‘globally indexed’’ refers to storage of an identical, sparse copy of the final matrix h_{ij}^{uc} across all MPI tasks. In the ‘‘globally indexed’’ case, the size of the stored array thus grows with system size on each MPI task, regardless of the number of MPI ranks

employed. In contrast, the term “locally indexed” refers to the storage on each MPI task of separate, dense matrix versions of only those integration contributions to h_{ij}^{uc} that are non-zero on the localized subset of grid points handled by that task. In the “locally indexed” case, the size of the stored array on each task thus remains bounded if the system size increases, as long as the number of MPI ranks is increased along with the system size.

3.3.3. Globally-Indexed Sparse Real-Space Hamiltonian

Shown in Figure 5a is a visualization of the globally-indexed sparse matrix format, in which each MPI task has a full copy of the real-space matrix along with associated indexing arrays. In FHI-aims, we use the CSR format for the sparse representation. Indexing from $h_{ij}^{uc}[B_\nu]$ to h_{ij}^{uc} in the globally-indexed CSR format requires two steps. First, the basis function index in $\text{nnz}(B_\nu)$ is mapped back to the basis function index in the set of all basis functions, i.e. the row/column indices of the matrix in Figure 4b are mapped back to the row/column indices of the matrix in Figure 4a. Second, the matrix element is mapped back to the sparse matrix representation used to store the real-space Hamiltonian matrix via indexing arrays.

Each process, after evaluating all batches assigned to it, has a local incomplete copy of the real-space Hamiltonian matrix

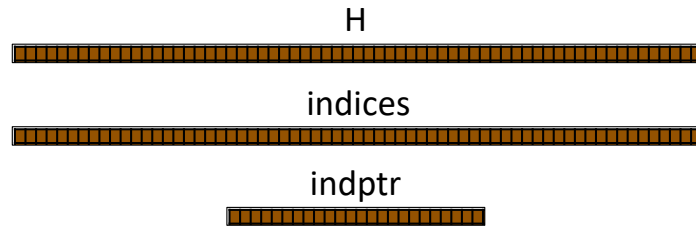
$$h_{ij}^{uc,\text{task}} = \sum_{B_\nu \text{ on task}} h_{ij}^{uc}[B_\nu]. \quad (28)$$

At the end of the RSDD algorithm, an in-place synchronization call sums up all local copies of h_{ij}^{uc} across processes,

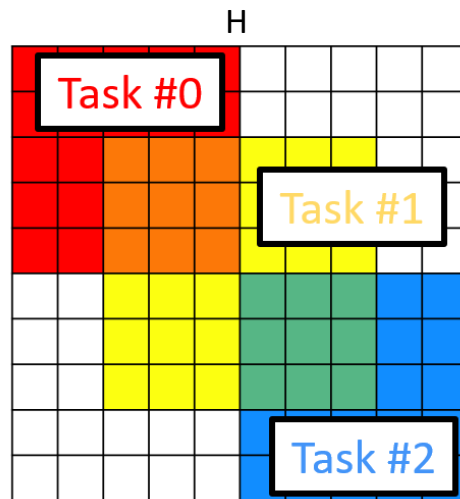
$$h_{ij}^{uc} = \sum_{\text{tasks}} h_{ij}^{uc,\text{task}}, \quad (29)$$

yielding the final values for the real-space Hamiltonian matrix synchronized across all processes. This is the only communication step in the RSDD algorithm.

The sparse matrix storage used in this matrix format makes it an efficient choice for smaller calculations. However, it has two key disadvantages impeding its usage for large-scale calculations and massively-parallel architectures. The sparse storage of h_{ij}^{uc} nevertheless scales as $O(N_{atom})$ on each MPI task and will be a memory bottleneck for large-scale systems, in particular ill-suited to reside in the on-board GPGPU memory. Additionally, the usage of non-trivial indexing arrays considerably impedes vectorization, making it ill-suited to the massively-vectorized GPGPU programming paradigm.



(a) Globally-Indexed Sparse



(b) Locally-Indexed Dense

Figure 5: Visualization of the two main matrix formats used for storing real-space matrices in FHI-aims. Subfigure (a) shows the globally-indexed sparse format, where each MPI task has a full copy of the matrix H in a sparse format (here, CSR) along with two indexing arrays `indices` and `indptr`. Subfigure (b) shows the locally-indexed dense format, where each MPI task has a partial section of the matrix in a dense format.

3.3.4. Locally-Indexed Dense Real-Space Hamiltonian

Shown in Figure 5b is a visualization of the locally-indexed dense matrix format, where h_{ij}^{uc} is distributed across processes. Each MPI task stores its portion of the integrals that contribute to h_{ij}^{uc} locally in a dense format – i.e., those partial integrals $h_{ij}^{uc,task}$ (Eq. 28) that are non-zero for this task. In short, only matrix elements involving basis functions with non-zero support on at least one batch on a given process, i.e. with support on the set $\cup_{B_\nu \text{ on task}} B_\nu$, are stored. The indexing step from $h_{ij}^{uc}[B_\nu]$ to $h_{ij}^{uc,task}$ is amenable to GPGPU resources due to the dense storage of $h_{ij}^{uc,task}$, amounting to a usage of a simple pre-calculated look-up table.

After the RSSD algorithm has concluded, the locally-index matrix elements $h_{ij}^{uc,task}$ are distributed across MPI tasks in an overlapping fashion, i.e. a given matrix element h_{ij}^{uc} may have non-zero contributions $h_{ij}^{uc,task}$ on multiple MPI tasks. Implementing Eq. (29) to convert these local matrices into a form h_{ij} (non-periodic systems) or $h_{ij}(\mathbf{k})$ (periodic systems) suitable for the eigensolver (here, BLACS for ELPA) is considerably more tedious than in the globally-indexed case, as book keeping to determine ownership of matrix elements and point-to-point communication between MPI tasks is required. Nevertheless, this synchronization step only occurs once and has negligible effect on the overall timings.

This dense matrix format consumes more memory than the globally-indexed sparse format for small calculations, as negligible matrix elements will be computed and stored in the local dense matrices. For sufficiently large calculations with sufficiently many MPI tasks, the distributed nature of this format is far more efficient in overall memory usage than the globally-indexed sparse format, and the resulting local dense matrices fit completely into GPGPU onboard memory, minimizing CPU-GPGPU communication.

3.3.5. Density and Density Derivatives, Force and Stress Tensor Components

In principle, all computational steps of other quantities derived from basis functions on the real-space grid can profit from very similar sparsity considerations as laid out for the Hamiltonian and overlap matrices above. This entails the density and its derivatives, which (cf. Eq. (3)) obey precisely the same locality constraints in each batch of grid points as the Hamiltonian and overlap matrices. The force and stress tensor components are likewise cast in the form of numerical integrals that, within each batch, are touched by only a bounded number of localized basis functions in the limit of large systems.

The computationally dominant operations for all these terms are, again, dense matrix multiplications. Since they can be carried out on the same set of distributed batches of grid points as the Hamiltonian and overlap matrices, the relevant index ranges (grid points in each batch and non-zero basis functions in each batch) are effectively identical to those in Eq. (27). Quantities are either kept on the distributed grid directly (density and its derivatives, which are local quantities) or (for forces and stress tensor components) the necessary integrals can be carried out by initially assembling matrix elements with basis functions as their indices. The process for the latter matrix elements is essentially identical to the detailed distribution strategy described above for the Hamiltonian matrix. Actual force and stress tensor components in terms of atomic coordinates can then be summed up from these matrix elements once, after the entire integration grid has been completely processed.

3.4. GPGPU Acceleration of the Real-Space Domain Decomposition Algorithm

Figure 6 shows pseudocode for the CPU-only and GPGPU-accelerated implementations of the real-space (a) Hamiltonian matrix integration and (b) electron density update. We refer to these two operations collectively as “the real-space operations” hereafter. The basic structure of the real-space operations consists of a loop over every batch assigned to the process, possibly followed by a final post-processed synchronization across all processes for integrals. No synchronization is necessary for the electron density update, as the real-space points where the electron density is defined are distributed across processes. For each batch assigned to a process, its contribution to the desired quantity is calculated. The processing of each batch can be broken up into three phases: initial processing where the necessary quantities (basis functions on each grid point, their gradients, etc.) are computed, a sequence of serial dense linear algebra operations (e.g., Eq. (27)), and a final indexing step to sort matrix contributions from each batch into their respective storage arrays on each MPI task.

Common to the initial processing phase for all real-space operations is the construction of the basis elements $\varphi_i \in \text{nnz}(B_\nu)$ for all $\mathbf{r} \in B_\nu$. The initial processing phase for the electron density update additionally includes the reduction of the density matrix of the full system (stored in a sparse representation) to the dense-but-smaller n_{ij} matrix as outlined in the previous section. The real-space Hamiltonian matrix integration requires that the

(a) **Hamiltonian Matrix Calculation**

$$h_{ij} = \int d\mathbf{r} [\varphi_i^*(\mathbf{r}) \hat{h}_{KS} \varphi_j(\mathbf{r})]$$

CPU-Only

```
do i_batch = 1, number_of_batches
  calculate_w( i_batch, w )
  calculate_phi( i_batch, phi )
  calculate_h_times_phi( i_batch, h_times_phi )

  phi(:) = w . phi(:)
  DSYR2K( h_times_phi, phi, h_batch )

  insert_into_h( h_batch, h )
end do
```

GPGPU-Accelerated

```
do i_batch = 1, number_of_batches
  calculate_w( i_batch, w )
  calculate_phi( i_batch, phi )
  calculate_h_times_phi( i_batch, h_times_phi )

  copy_cpu_data_to_gpu( w, phi, h_times_phi )
  cublasDDGMM( phi, w, phi )
  cublasDSYR2K( h_times_phi, phi, h_batch )

  insert_into_h_gpu( h_batch, h )
end do

copy_gpu_data_to_cpu( h )
```

(b) **Electron Density Calculation**

$$n(\mathbf{r}) = \sum_{ij} \varphi_i^*(\mathbf{r}) n_{ij} \varphi_j(\mathbf{r})$$

CPU-Only

```
do i_batch = 1, number_of_batches
  calculate_phi( i_batch, phi )
  calculate_density_mat( i_batch, density_mat )

  DSYMM( density_mat, phi, temp )
  n_batch = temp . phi

  insert_into_n( n_batch, n )
end do
```

GPGPU-Accelerated

```
do i_batch = 1, number_of_batches
  calculate_phi( i_batch, phi )
  calculate_density_mat( i_batch, density_mat )

  copy_cpu_data_to_gpu( density_mat, phi )
  cublasDSYMM( density_mat, phi, temp )
  cublasDDGMM( temp, phi, n_batch )

  insert_into_n_gpu( n_batch, n )
end do

copy_gpu_data_to_cpu( h )
```

Figure 6: Pseudocode comparing CPU-only and GPGPU-accelerated implementations of the RSDD algorithms in FHI-aims for the (a) real-space Hamiltonian matrix calculation and (b) electron density calculation. The evaluation of the tau matrix for meta-GGAs has been omitted in (a) for brevity. It is calculated via a single DGEMM/cublasDDGMM call and added to the h_{ij}^{uc} matrix at the end of each loop iteration. In (a), the final summation of all partial contributions to h_{ij}^{uc} across different MPI tasks happens either immediately after the pseudocode shown (globally indexed version) or later (locally indexed version), when the full matrix elements $h_{ij}(\mathbf{k})$ of Eq. (11) are constructed from Bloch phase factors and partially summed versions of h_{ij}^{uc} stored on each separate MPI task.

pre-computed integration point weights be re-indexed for the current batch and the quantities $\{\hat{h}_{KS}\varphi_i(\mathbf{r})\}$ be evaluated on every point in B_ν for all basis elements in $\text{nnz}(B_\nu)$.

The construction of $\{\varphi_i(\mathbf{r})\}$, and $\{\hat{h}_{KS}\varphi_i(\mathbf{r})\}$ for each point on a batch is executed per point, with relatively small workload compared to the final DGEMMs, but with some thread-divergent branching statements during the construction, i.e. not immediately suitable for GPGPUS. As we will see below, for the integrals, we can overlay this work on the CPU while the GPU works on something else.

The dense linear algebra phase consists of two subroutine calls for Hamiltonian integration: a matrix multiplication (DSYR2K for the real-space Hamiltonian matrix and DSYMM for the electron density) and a dot product. This step is offloadable to the GPGPU at the cost of communication of the quantities previously calculated during the initial processing phase: the integration weights $w(\mathbf{r})$, basis functions $\{\varphi_i(\mathbf{r})\}$, and $\{\hat{h}_{KS}\varphi_i(\mathbf{r})\}$ matrix for the real-space Hamiltonian integration in Eq. (22), and the basis functions φ and batch subspace restricted density matrix n_{ij} for the electron density in Eq. (3).

The final phase for each loop iteration is an indexing phase, where the results from the dense linear algebra phase $h_{ij}^{uc}[B_\nu]$ are indexed back into the accumulated matrices h_{ij}^{uc} . The GPGPU acceleration strategy for the real-space Hamiltonian integration diverges based on the choice of indexing for the Hamiltonian matrix h_{ij}^{uc} :

(i) The globally-indexed CSR format uses several thread-divergent branching conditionals, complicating GPGPU acceleration of the indexing. The GPGPU-accelerated algorithm thus communicates the results of the dense linear algebra step for each batch back to the CPU, which performs the indexing. In this approach, the CPU is idle while the GPGPU evaluates the dense linear algebra for each batch.

(ii) Alternatively, when using the locally-indexed dense storage format for h_{ij}^{uc} , indexing is embarrassingly parallelizable, allowing for the usage of custom CUDA kernels to perform the indexing on the GPGPU. After the CPU has communicated $\{\varphi_i(\mathbf{r})\}$ and $\{\hat{h}_{KS}\varphi_i(\mathbf{r})\}$ to the GPGPU, it is free to begin calculating $\{\varphi_i(\mathbf{r})\}$ and $\{\hat{h}_{KS}\varphi_i(\mathbf{r})\}$ for the next batch, allowing for effective overlay of computation between the CPU and GPGPU. Communication from the GPGPU back to the CPU occurs only once at the end of the algorithm, when the GPGPU communicates its copy of h_{ij}^{uc} back to the CPU.

A similar approach to (ii) is employed when calculating the electron density or its derivatives, as the mapping from real-space points $\mathbf{r} \in B_\nu$ to the set of all integration points assigned to the present process $\cup_{B_\nu \text{ on task}} B_\nu$ is trivial. This permits the electron density indexing to be performed via a simple CUDA kernel and stored on the GPGPU locally, similarly avoiding communication from the GPGPU back to the CPU communication for each batch. The electron density stored on the GPGPU is communicated back to the CPU at the end of the algorithm.

4. Results

All benchmark calculations were performed with the full-potential, all-electron FHI-aims electronic structure code [30, 37] using its production-quality “tight” basis sets and “tight” real-space integration grids and Hartree potential. The PBE functional [101] was used to model exchange-correlation effects. We use a Γ -point-only k-grid in this work, as we focus on real-space operations whose timings are independent of the selected reciprocal-space grid. All timings shown use the locally-indexed dense matrix format (Figure 5b) for the Hamiltonian integration and forces/stress evaluation. The choice of “tight” settings is important since the larger workload associated with denser grids and larger basis sets can dominate the overall effort associated with a particular DFT-based simulation project. By construction, larger workloads of this kind also benefit more from GPGPU acceleration. For progressively lighter settings, smaller but still useful speedups would be expected. The benchmarks below reflect the highest-cost parts of a routine simulation where, it turns out, GPU acceleration will most efficiently take off the edge of a very large workload.

The time-intensive operations for semi-local DFT in FHI-aims are the real-space Hamiltonian integration (Eq. (10) or (12)), density update (Eq. (3)), Hartree potential calculation (Eq. (9)), and the solution of the Kohn-Sham eigenvalue equation (Eq. (13)).

Figure 1 shows a schematic for the program flow of a standard KS-DFT calculation with geometry relaxation or molecular dynamics. First, the electronic structure for current geometry is converged by iterative calculation of the Hartree potential (9), Hamiltonian operator (Eq. (1)), Hamiltonian matrix elements (Eq. (10) or 11), and electron density via the Kohn-Sham eigenvalue equation (Eqs. (3) and (13)). We denote a single collective iteration of these operations in which the electronic structure is updated as a

“standard” SCF iteration.

Once self-consistency is reached in the electronic structure, \mathbf{F}_{at} and $\sigma_{\lambda\mu}$ may be calculated by Eqs. (14) and (20) respectively. The implementation of Eqs. (14) and (20) in FHI-aims are published in [30, 83]; here, it is sufficient to highlight two contributions to \mathbf{F}_{at} and $\sigma_{\lambda\mu}$ which contribute appreciably to timings:

- The Hellmann-Feynman contribution to \mathbf{F}_{at} and $\sigma_{\lambda\mu}$ is calculated alongside the Hartree multipole summation, as it relies on the Hartree potential of the system. Thus, the domain decomposition strategy is not used for evaluating this contribution, and GPGPU acceleration is not employed.
- The Pulay contribution to \mathbf{F}_{at} and $\sigma_{\lambda\mu}$ is calculated alongside the density update, as it relies on the density matrix n_{ij} and the energy-weighted density matrix q_{ij} . The domain decomposition strategy is used for evaluating this contribution. Its evaluation is GPGPU-accelerated using the strategy outlined in Section 3.4.

While the calculations of these quantities are computationally expensive, they are ideally evaluated only once per geometry step (outer loop of Figure 1), whereas the SCF iterations will be evaluated multiple times per geometry step (inner loop of Figure 1).

In principle, the electronic structure should be further iterated until \mathbf{F}_{at} and $\sigma_{\lambda\mu}$ have converged. The production settings for FHI-aims are sufficiently tight that in practice only a single calculation of \mathbf{F}_{at} and $\sigma_{\lambda\mu}$ are needed at the end of each self-consistency cycle. The geometry is then updated using \mathbf{F}_{at} and $\sigma_{\lambda\mu}$.

Accordingly, we benchmark three different types of SCF iterations in this paper:

- “SCF”: a single iteration of the SCF cycle loop,
- “SCF + \mathbf{F}_{at} ”: a single iteration of the SCF cycle loop followed by the computation of forces \mathbf{F}_{at} , and
- “SCF + \mathbf{F}_{at} + $\sigma_{\lambda\mu}$ ”: a single iteration of the SCF cycle loop followed by the computation of forces \mathbf{F}_{at} and stress tensor $\sigma_{\lambda\mu}$.

Node Type	IvyBridge/GP100	Haswell/P100	Skylake/V100	POWER9/V100
Computer Cluster	timewarp	PSG	PSG	LLNL’s Lassen
CPU	2x Intel Xeon E5-2670v2 (20 cores, Ivy Bridge)	2x Intel Xeon E5-2698v3 (32 cores, Haswell)	2x Intel Xeon Gold 6148 (20 cores, Skylake)	2x IBM POWER9 AC922 (40 cores, POWER9)
GPGPU	1x Quadro GP100 (Pascal)	4x Tesla P100 (Pascal)	4x Tesla V100 (Volta)	4x Tesla V100 (Volta)
MPI Tasks/GPGPUs	16/1	32/4	20/4	40/4
Compilers/Libraries	ifort 14.0, MKL 11.1.1, IMPI 4.1.3, CUDA 8.0	ifort 17.0, MKL 11.3.3, IMPI 5.0.3, CUDA 9.1	ifort 17.0, MKL 11.3.3, IMPI 5.0.3, CUDA 9.1	XL 2019.02.07, ESSL 6.1, Spectrum MPI, CUDA 9.2

Table 1: Per-node configurations for architectures used in this work.

We emphasize that these timings are per iteration, not per cycle. As outlined in Figure 1, a given system geometry loop will contain multiple iterations of “SCF” but ideally only one iteration of “SCF + \mathbf{F}_{at} ” or “SCF + $\mathbf{F}_{at} + \sigma_{\lambda\mu}$ ” per geometry step.

We cover a broad range of GPGPU-accelerated architectures by performing benchmarks on four different architectures provided by three different computing clusters: a local cluster (“timewarp”) at Duke University, a dedicated testing cluster (“PSG”) at NVIDIA Corporation, and the Lassen supercomputer at Lawrence Livermore National Laboratory (“LLNL”). The hardware architectures, which we categorize based on CPU and GPU generations, are IvyBridge/GP100 [timewarp], Haswell/P100 [PSG], Skylake/V100 [PSG], and POWER9/V100 [LLNL]. More information on architectures may be found in Table 1. Full node utilization was employed for all architectures except on IvyBridge/GP100 [timewarp], where 16 MPI tasks were used (out of the 20 physical cores) due to limitations imposed on Pascal GPGPUs by the NVIDIA MPS service, which was used to distribute the computational load to the GPGPU.

We consider two types of timings for a given operation in this work, the timing t_{CPU} for an operation when employing all available CPU cores on a given node using the Message Passing Interface (MPI), and the timings t_{GPGPU} for an operation when GPGPU acceleration has been employed alongside full CPU node utilization. The GPGPU-accelerated speedup, or simply “speedup”, is then defined as

$$s = t_{CPU}/t_{GPGPU}. \quad (30)$$

Using this definition, identical timings for CPU-only and GPGPU-accelerated

operations correspond to a speedup of $s = 1.0$. We note specifically that this is a hard comparison, in that the GPU+CPU timings must be better than a computation using all CPU cores on a given, state-of-the-art node to show a net speedup.

4.1. Materials Used

Two different sets of materials are considered in this work:

- The first set of materials is a benchmark set comprising 103 different inorganic compounds (bulk solids), proposed in [91]. The compounds in this benchmark set span 66 chemical elements in 10 structural prototypes, providing a broad coverage of the structural and chemical diversity found in real-world condensed-matter simulations. $3 \times 3 \times 3$ supercells of the primitive cell for each material were used, leading to cell sizes of 27, 54, and 108 atoms. In addition to discussing averaged / aggregated data, we highlight timings for the 54-atom diamond Si supercell calculation as a particular example in the body of this text. The benchmark set is investigated on a single node of three out of the four architectures listed in Table 1, namely the IvyBridge/GP100 [time-warp], Haswell/P100 [PSG], and Skylake/V100 [PSG] architectures.
- The second set of materials consists of a 5×5 supercell of a 2D Bi_2Se_3 bilayer. A vacuum thickness of 40 Å was used. In a standard FHI-aims calculation, the vacuum thickness contributes to timings only through the reciprocal-space contribution of the Ewald summation [102, 30] used to evaluate the electrostatic potential to the Hartree potential. Calculations for the Bi_2Se_3 bilayer were performed on the POWER9/V100 [LLNL] architecture using 2 to 128 nodes.

4.2. GPGPU Acceleration Across Materials and Architectures

Table 2 shows a comparison of timings computed on the Skylake/V100 [PSG] architecture for diamond Si. The evaluation of the electron density and its gradients is the dominant contribution to the total time for all SCF iteration types. The relative weight of the density calculation increases for SCF iterations involving \mathbf{F}_{at} and $\sigma_{\lambda\mu}$ as the evaluation of the Pulay contribution must also be performed in this step. For an SCF + \mathbf{F}_{at} + $\sigma_{\lambda\mu}$ iteration, 95% of the calculation time is spent calculating the density and the Pulay contribution to \mathbf{F}_{at} + $\sigma_{\lambda\mu}$. The timing for Hartree summation weakly increases for SCF cycles involving \mathbf{F}_{at} as the Hellmann-Feynman forces must

Operation	Timing Type	SCF	SCF + \mathbf{F}_{at}	SCF + \mathbf{F}_{at} + $\sigma_{\lambda\mu}$
Integration (Eq. (12))	t_{CPU} (s)	10.4	10.3	10.4
	t_{GPGPU} (s)	1.6	1.6	1.6
Hartree Summation (Eq. (9)) + Hellmann-Feynman (Eqs. (14), (20))	t_{CPU} (s)	4.3	16.6	20.2
Electron Density (Eq. (3)) + Pulay (Eqs. (14), (20))	t_{CPU} (s)	20.7	243.7	565.2
	t_{GPGPU} (s)	5.3	29.2	54.5
Total Time for Iteration	t_{CPU} (s)	35.5	270.8	596.0
	t_{GPGPU} (s)	11.6	47.7	76.5

Table 2: Timings for various CPU-only and GPGPU-accelerated operations computed on the Skylake/V100 [PSG] architecture for a 54-atom Si supercell (diamond structure). Only t_{CPU} is presented for the Hartree summation and Hellmann-Feynman contributions to \mathbf{F}_{at} and $\sigma_{\lambda\mu}$, as GPGPU acceleration is not employed for these calculations. All timings were taken from a single calculation.

be calculated, but this is a comparatively small expense relative to the time required to compute the Pulay terms. In contrast, the Hamiltonian integration does not include \mathbf{F}_{at} or $\sigma_{\lambda\mu}$ components, leading to consistent timings across iteration types.

For all three iteration types, when GPGPU acceleration is enabled, there is a consistent $s=6.4$ speedup in the Hamiltonian integration on the Skylake/V100 [PSG] architecture. Differences in the GPGPU performance are observed when calculating the density, its gradients, and potentially the Pulay contributions to forces and stress. Speedups of 3.9, 8.4, and 10.4 are observed in the density calculation on the Skylake/V100 [PSG] architecture for the standard SCF, SCF + \mathbf{F}_{at} , and SCF + \mathbf{F}_{at} + $\sigma_{\lambda\mu}$ iterations, respectively. The differences in speedups arise from the increased workload of dense linear algebra performed when calculating the Pulay contribution to \mathbf{F}_{at} and $\sigma_{\lambda\mu}$. The computationally more demanding iterations with more dense linear algebra exhibit greater GPGPU-accelerated improvements for timings in both relative and absolute terms. Speedups for the total times of an iteration show a similar trend to the density update, with speedups of 3.1, 5.7, and 7.8 observed on the Skylake/V100 [PSG] architecture for the three SCF iteration types. The density update dominates the runtimes for the iterations.

Table 3 extends the analysis to the IvyBridge/GP100 [timewarp] and Haswell/P100 [PSG] architectures with a comparison of total times for the three types of iterations. The three architectures show similar trends; speedups increase as the linear algebra workload increases, with speedups of 2.9, 4.4, and 5.2 observed for IvyBridge/GP100 [timewarp] and 2.5, 5.8, and 6.7 ob-

Architecture	Timing Type	SCF	SCF + \mathbf{F}_{at}	SCF + \mathbf{F}_{at} + $\sigma_{\lambda\mu}$
IvyBridge/GP100 [timewarp]	t_{CPU} (s)	77.7	545.0	1130.5
	t_{GPGPU} (s)	26.5	123.3	218.8
Haswell/P100 [PSG]	t_{CPU} (s)	38.5	315.2	682.0
	t_{GPGPU} (s)	15.4	54.3	101.3
Skylake/V100 [PSG]	t_{CPU} (s)	35.5	270.8	596.0
	t_{GPGPU} (s)	11.6	47.7	76.5

Table 3: Comparison of total timings for iterations across different architectures for a 54-atom Si supercell (diamond structure). All timings were taken from a single calculation.

served for Haswell/P100 [PSG]. The trends in speedups observed on Skylake/V100 [PSG] hold for other GPGPU-accelerated architectures.

While an individual SCF + \mathbf{F}_{at} + $\sigma_{\lambda\mu}$ iteration benefits greatly from GPGPU acceleration and takes considerably more time than a standard SCF iteration, it is calculated only when self-consistency is reached and often only needs to be calculated once (Fig. 1). On the other hand, there will be multiple standard SCF iterations, which show a reduced GPGPU speedup. To assess the impact of this difference in speedups on the overall timing of a calculation, Figure 7 shows the timings for complete calculations for diamond Si on IvyBridge/GP100 [timewarp], Haswell/P100 [PSG], and Skylake/V100 [PSG] architectures. Self-consistency is reached after 12 standard SCF iterations and one SCF + \mathbf{F}_{at} + $\sigma_{\lambda\mu}$ iteration, leading to speedups between 3.7 and 4.0 for the total time of the calculation.

We next turn our attention to the 103 material benchmark set. To compare results from different materials, we estimate the expected workload for a given material using a metric

$$\begin{aligned}
 \# \text{ ops} &= \#B_\nu * MM & (31) \\
 MM &= \langle |B_\nu| \rangle * \langle \text{nnz}(B_\nu) \rangle^2
 \end{aligned}$$

where $\langle |B_\nu| \rangle$ is the average number of points per batch for a material, $\langle \text{nnz}(B_\nu) \rangle$ is the average number of basis functions with non-zero support per batch for a material, and $\#B_\nu$ is the number of batches for a material. The quantity MM is then a measure of the timing for a hypothetical real-space operation involving a single matrix multiplication, and $\# \text{ ops}$ is a measure of the total time of the real-space operation across all batches. As motivated by Eq. (27), and as we show below, this metric will give an approximate estimate for the expected workload, as it is expected to map particularly the dominant part



Figure 7: Overall timings across architectures for the calculation for a 54-atom Si supercell (diamond structure). All calculations contain initialization, 12 SCF iterations, and 1 SCF + \mathbf{F}_{at} + $\sigma_{\lambda\mu}$ iteration. Importantly, this also contains all non-GPU accelerated parts of the calculation

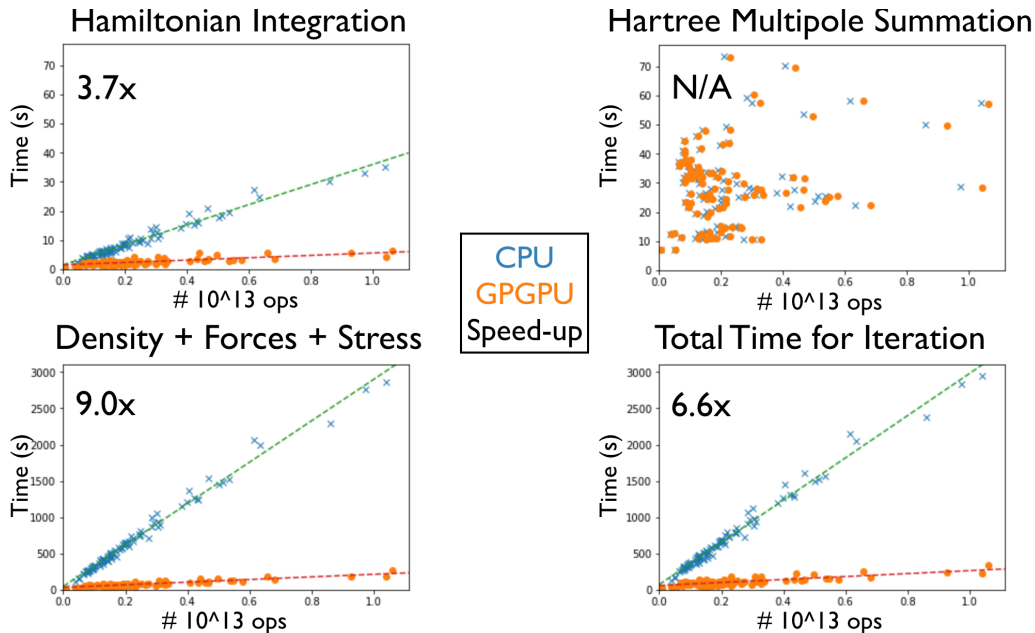


Figure 8: Timings for various operations in an SCF + forces + stress tensor iteration across the 103 material benchmark set for the (a) Hamiltonian integration, (b) Hartree multipole summation and Hellman-Feynman forces, (c) density and Pulay contributions to forces and stress tensor, culminating in (d) the total time for the iteration. The Skylake/V100 [PSG] architecture was used.

of the workload associated with dense serial matrix multiplications with high accuracy.

Shown in Figure 8 are timings for an SCF + \mathbf{F}_{at} + $\sigma_{\lambda\mu}$ iteration calculated using Skylake/V100 [PSG]. The proposed metric correlates well to the timings observed for real-space operations in FHI-aims. A strong linear trend for the Hamiltonian integration (Fig. 8a) and density + force + stress evaluation (Fig. 8c) is observed, reflecting the relatively significant workload of dense linear algebra in these operations. The total time for an iteration (Fig. 8d) shows a similar trend, as it is dominated by the density + force + stress evaluation. No such trend is observed in the Hartree multipole summation, which does not rely on dense linear algebra and is also not yet GPU accelerated in the present work.

Average speedups of 3.7, 9.0, and 6.6 are observed for Hamiltonian integration, density evaluation, and the total time for an SCF + \mathbf{F}_{at} + $\sigma_{\lambda\mu}$ iteration for the 103 material benchmark set. These speedups are consistent

Architecture	SCF	SCF + \mathbf{F}_{at}	SCF + \mathbf{F}_{at} + $\sigma_{\lambda\mu}$
IvyBridge/GP100 [timewarp]	2.4	3.9	4.5
Haswell/P100 [PSG]	2.1	4.5	6.6
Skylake/V100 [PSG]	2.4	6.6	6.6

Table 4: Comparison of speedups for iterations across different architectures for the 103 material benchmark set.

with the speedups observed for diamond Si. Table 4 shows a comparison across architectures for the speedups calculated for the 103 material benchmark set. These results are analogous to the results in Table 3, indicating that our analysis of trends observed in the diamond Si system extends to other materials and other architectures as well.

4.3. Strong Scaling for CPU-Only and GPGPU-Accelerated Calculations

The calculations in the previous section were performed using a fixed number of MPI tasks on a single node. In the present section, we assess the scaling across nodes using a 375-atom Bi_2Se_3 bilayer system as a larger example. Strong scaling plots for the POWER9/V100 [LLNL] architecture are shown in Figure 9, with subfigure (a) showing a standard SCF iteration and subfigure (b) showing an SCF + \mathbf{F}_{at} + $\sigma_{\lambda\mu}$ iteration. Timings for 80, 160, 320, 640, 1280, 2560, and 5120 MPI tasks are presented, and we reintroduce the timings for the solution of the Kohn-Sham eigenvalue equation. The slab geometry corresponds to a (5×5) supercell, using FHI-aims’ “tight” production settings (17,850 basis functions total) and a Γ -point only calculation is performed. The calculations shown correspond to scalar-relativistic self-consistency iterations for this system, i.e., the workload that constitutes the bulk of a typical DFT calculation for such a system. As shown in [91] and others, the energy band structure of such a system is subject to spin-orbit coupling effects that would be essential to include at least at a post-processed second-variational (i.e., perturbative) level for qualitatively correct results. The necessary spin-orbit coupled Hamiltonian matrix integrals follow the exact same algorithms as those of the scalar-relativistic integrations shown in Fig. 9(a) and are therefore not repeated in detail in the plots.

Timings for the Bi_2Se_3 bilayer are dominated by the real-space density update and potentially forces and stresses, consistent with the results from

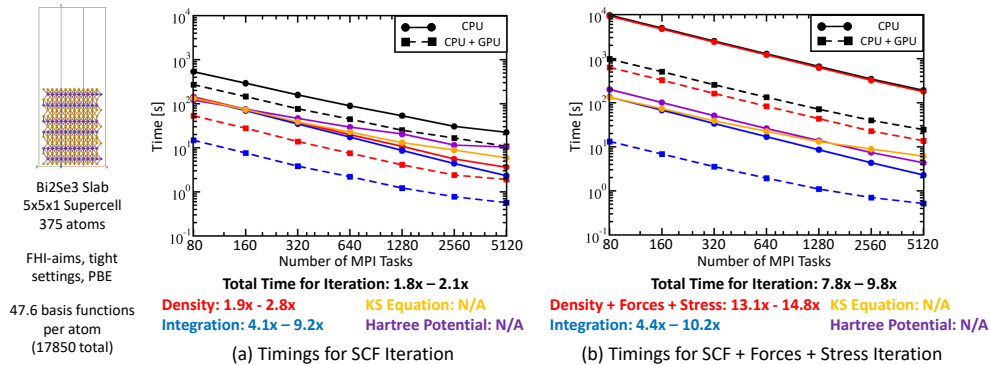


Figure 9: Timings on LLNL’s Lassen for a 375-atom Bi₂Se₃ bilayer with a 40 Å vacuum for (a) an SCF iteration and (b) an SCF iteration including the calculation of forces and the stress tensor.

the previous section. GPGPU-accelerated speedups of 1.8 - 2.1 and 7.8 - 9.8 are observed for overall timings in a standard SCF iteration and SCF + \mathbf{F}_{at} + $\sigma_{\lambda\mu}$ iterations, respectively. Real-space operations show ideal scaling as a function of the number of MPI tasks, as is expected for the domain decomposition algorithm. The solution of the Kohn-Sham matrix eigenvalue problem using the ELPA library [92, 77, 79, 78] (not GPU-accelerated in Fig. 9) shows reduced scaling due to the still relatively small matrix dimension size, but its diminished weight in these calculations does not meaningfully impact the overall scaling of the calculations. A denser k -space grid (e.g., $2 \times 2 \times 1$ or $4 \times 4 \times 1$) would increase the eigenvalue solver related workload and could be accelerated, e.g. by the recently published distributed-parallel, GPGPU-accelerated one-stage ELPA solver [79, 78] (a computational step that is separate and independent of the real-space operations reported in this work).

5. Conclusion

In this paper, we show GPGPU acceleration for real-space operations relevant in semilocal DFT for production-quality materials simulations. We particularly focus on the domain decomposition method used by the full-potential, all-electron FHI-aims electronic structure code for real-space operations. We show that the time-intensive portions of the domain decomposition method are dense linear algebra operations which are bounded in memory consumption, allowing for efficient offloading to GPGPU resources.

The performance of the GPGPU acceleration in FHI-aims was assessed using a 103-material benchmark set on three heterogeneous CPU-GPGPU architectures. GPGPU-accelerated speedups ranging from $s = 2.4$ for SCF iterations to $s = 6.6$ for SCF iterations including evaluation of forces \mathbf{F}_{at} and the stress tensor $\sigma_{\lambda\mu}$ were observed, with an overall estimated speedup of $s \approx 3 - 4$ expected for total times for entire calculations.

Scaling on HPC resources was assessed on LLNL’s Lassen calculations involving a 375-atom Bi_2Se_3 slab supercell. The GPGPU-accelerated implementation shows near-ideal scaling similar to the CPU-only implementation. We find that the evaluation of the density, forces, and stress tensors is the dominant computational workload for the 375-atom bilayer, allowing for overall GPGPU-accelerated speedups of $s \approx 8-10$. For significantly larger systems, the well-known cubic bottleneck of the Kohn-Sham DFT equation (the eigenvalue solver, which is not GPGPU-accelerated in this work) would begin to dominate the computational workload. However, a large subset of electronic structure computational needs in the range of small and mid-sized problems (below the range in which the eigenvalue solver dominates, i.e., up to several hundred atoms in this work) becomes accessible to GPGPU acceleration using the localized basis set strategies described above.

6. Acknowledgements

This work was supported by the LDRD Program of ORNL managed by UT-Battelle, LLC, for the U.S. DOE and by the Oak Ridge Leadership Computing Facility, which is a DOE Office of Science User Facility supported under Contract DE-AC05-00OR22725. A portion of work was conducted at the Center for Nanophase Materials Sciences, which is a DOE Office of Science User Facility, and supported by the Creative Materials Discovery Program through the National Research Foundation of Korea funded by the Ministry of Science, ICT and Future Planning (NRF-2016M3D1A1919181). We gratefully acknowledge the support of NVIDIA Corporation with the donation of Quadro GP100 and Titan V GPGPUs used for local development, as well as access to their PSG cluster. We thank Dr. Vincenzo Lordi and the Lawrence Livermore National Laboratory (LLNL), a U.S. Department of Energy Facility, for assistance with and access to LLNL’s supercomputer Lassen for benchmarks conducted in this work. The work on LLNLs Lassen supercomputer was performed under the auspices of the U.S. Department of Energy at Lawrence Livermore National Laboratory under Contract No. DE-

AC52-07NA27344. We would finally like to acknowledge the contribution of Dr. Rainer Johanni, deceased in 2012, who pioneered the distributed-parallel CPU version of the locally-indexed real-space Hamiltonian scheme that is a critical foundation of this work.

References

- [1] P. Hohenberg, W. Kohn, Inhomogeneous electron gas, *Phys. Rev.* 136 (3B) (1964) 864–871. doi:10.1103/PhysRev.136.B864.
- [2] W. Kohn, L. J. Sham, Self-consistent equations including exchange and correlation effects, *Phys. Rev.* 140 (4A) (1965) 1133–1138. doi:10.1103/PhysRev.140.A1133.
- [3] K. Burke, Perspective on density functional theory, *J. Chem. Phys.* 136 (2012) 150901. doi:10.1063/1.4704546.
- [4] R. O. Jones, Density functional theory: Past, present, ... future?, Ψ_k Newsletter 124 (2014) 1–23.
- [5] A. D. Becke, Perspective: Fifty years of density-functional theory in chemical physics, *J. Chem. Phys.* 140 (2014) 18A301. doi:10.1063/1.4869598.
- [6] A. Jain, Y. Shin, K. A. Persson, Computational predictions of energy materials using density functional theory, *Nature Rev. Mater.* 1 (2016) 1–13. doi:10.1038/natrevmats.2015.4.
- [7] M. J. Frisch, J. A. Pople, J. S. Binkley, Self-consistent molecular orbital methods 25. Supplementary functions for Gaussian basis sets, *J. Chem. Phys.* 80 (7) (1984) 3265–3269. doi:10.1063/1.447079.
- [8] T. H. Dunning, Gaussian basis sets for use in correlated molecular calculations. I. The atoms boron through neon and hydrogen, *J. Chem. Phys.* 90 (2) (1989) 1007–1023. doi:10.1063/1.456153.
- [9] A. Szabo, N. S. Ostlund, *Modern Quantum Chemistry: Introduction to Advanced Electronic Structure Theory*, 1st Edition, Dover Publications, Mineola, NY, 1996.

- [10] A. K. Wilson, T. van Mourik, T. H. Dunning, Gaussian basis sets for use in correlated molecular calculations. VI. Sextuple zeta correlation consistent basis sets for boron through neon, *J. Mol. Struct.* 388 (1996) 339–349. doi:10.1016/S0166-1280(96)80048-0.
- [11] F. Weigend, R. Ahlrichs, Balanced basis sets of split valence, triple zeta valence and quadruple zeta valence quality for H to Rn: Design and assessment of accuracy, *Phys. Chem. Chem. Phys.* 7 (2005) 3297–3305. doi:10.1039/b508541a.
- [12] M. Valiev, E. J. Bylaska, N. Govind, K. Kowalski, T. P. Straatsma, H. J. J. Van Dam, D. Wang, J. Nieplocha, E. Apra, T. L. Windus, W. A. de Jong, NWChem: A comprehensive and scalable open-source solution for large scale molecular simulations, *Comput. Phys. Commun.* 181 (2010) 1477–1489. doi:10.1016/j.cpc.2010.04.018.
- [13] J. Hutter, M. Iannuzzi, F. Schiffmann, J. VandeVondele, cp2k: atomistic simulations of condensed matter systems, *WIREs Comput. Mol. Sci.* 4 (2014) 15–25. doi:10.1002/wcms.1159.
- [14] F. Furche, R. Ahlrichs, C. Hättig, W. Klopper, M. Sierka, F. Weigend, Turbomole, *WIREs Comput. Mol. Sci.* 4 (2014) 91–100. doi:10.1002/wcms.1162.
- [15] Y. Shao, Z. Gan, E. Epifanovsky, A. T. Gilbert, M. Wormit, J. Kussmann, A. W. Lange, A. Behn, J. Deng, X. Feng, D. Ghosh, M. Goldey, P. R. Horn, L. D. Jacobson, I. Kaliman, R. Z. Khaliullin, T. Kuś, A. Landau, J. Liu, E. I. Proynov, Y. M. Rhee, R. M. Richard, M. A. Rohrdanz, R. P. Steele, E. J. Sundstrom, H. L. Woodcock III, P. M. Zimmerman, D. Zuev, B. Albrecht, E. Alguire, B. Austin, G. J. O. Beran, Y. A. Bernard, E. Berquist, K. Brandhorst, K. B. Bravaya, S. T. Brown, D. Casanova, C.-M. Chang, Y. Chen, S. H. Chien, K. D. Closser, D. L. Crittenden, M. Diedenhofen, R. A. DiStasio Jr., H. Do, A. D. Dutoi, R. G. Edgar, S. Fatehi, L. Fusti-Molnar, A. Ghysels, A. Golubeva-Zadorozhnaya, J. Gomes, M. W. Hanson-Heine, P. H. Harbach, A. W. Hauser, E. G. Hohenstein, Z. C. Holden, T.-C. Jagau, H. Ji, B. Kaduk, K. Khistyayev, J. Kim, J. Kim, R. A. King, P. Klunzinger, D. Kosenkov, T. Kowalczyk, C. M. Krauter, K. U. Lao, A. D. Laurent, K. V. Lawler, S. V. Levchenko, C. Y. Lin, F. Liu,

E. Livshits, R. C. Lochan, A. Luenser, P. Manohar, S. F. Manzer, S.-P. Mao, N. Mardirossian, A. V. Marenich, S. A. Maurer, N. J. Mayhall, E. Neuscamman, C. M. Oana, R. Olivares-Amaya, D. P. O'Neill, J. A. Parkhill, T. M. Perrine, R. Peverati, A. Prociuk, D. R. Rehn, E. Rosta, N. J. Russ, S. M. Sharada, S. Sharma, D. W. Small, A. Sodt, T. Stein, D. Stück, Y.-C. Su, A. J. Thom, T. Tsuchimochi, V. Vanovschi, L. Vogt, O. Vydrov, T. Wang, M. A. Watson, J. Wenzel, A. White, C. F. Williams, J. Yang, S. Yeganeh, S. R. Yost, Z.-Q. You, I. Y. Zhang, X. Zhang, Y. Zhao, B. R. Brooks, G. K. L. Chan, D. M. Chipman, C. J. Cramer, W. A. Goddard III, M. S. Gordon, W. J. Hehre, A. Klamt, H. F. Schaefer III, M. W. Schmidt, C. D. Sherrill, D. G. Truhlar, A. Warshel, X. Xu, A. Aspuru-Guzik, R. Baer, A. T. Bell, N. A. Besley, J.-D. Chai, A. Dreuw, B. D. Dunietz, T. R. Furlani, S. R. Gwaltney, C.-P. Hsu, Y. Jung, J. Kong, D. S. Lambrecht, W. Liang, C. Ochsenfeld, V. A. Rassolov, L. V. Slipchenko, J. E. Subotnik, T. Van Voorhis, J. M. Herbert, A. I. Krylov, P. M. W. Gill, M. Head-Gordon, *Advances in molecular quantum chemistry contained in the Q-Chem 4 program package*, *Mol. Phys.* 113 (2) (2015) 184–215. doi:10.1080/00268976.2014.952696.

- [16] M. J. Frisch, G. W. Trucks, H. B. Schlegel, G. E. Scuseria, M. A. Robb, J. R. Cheeseman, G. Scalmani, V. Barone, G. A. Petersson, H. Nakatsuji, X. Li, M. Caricato, A. V. Marenich, J. Bloino, B. G. Janesko, R. Gomperts, B. Mennucci, H. P. Hratchian, J. V. Ortiz, A. F. Izmaylov, J. L. Sonnenberg, D. Williams-Young, F. Ding, F. Lipparini, F. Egidi, J. Goings, B. Peng, A. Petrone, T. Henderson, D. Ranasinghe, V. G. Zakrzewski, J. Gao, N. Rega, G. Zheng, W. Liang, M. Hada, M. Ehara, K. Toyota, R. Fukuda, J. Hasegawa, M. Ishida, T. Nakajima, Y. Honda, O. Kitao, H. Nakai, T. Vreven, K. Throssell, J. A. Montgomery, Jr., J. E. Peralta, F. Ogliaro, M. J. Bearpark, J. J. Heyd, E. N. Brothers, K. N. Kudin, V. N. Staroverov, T. A. Keith, R. Kobayashi, J. Normand, K. Raghavachari, A. P. Rendell, J. C. Burant, S. S. Iyengar, J. Tomasi, M. Cossi, J. M. Millam, M. Klene, C. Adamo, R. Cammi, J. W. Ochterski, R. L. Martin, K. Morokuma, O. Farkas, J. B. Foresman, D. J. Fox, *Gaussian 16 Revision B.01*, Gaussian Inc. Wallingford CT (2016).
- [17] S. R. Jensen, S. Saha, J. A. Flores-Livas, W. Huhn, V. Blum,

- S. Goedecker, L. Frediani, The elephant in the room of density functional theory calculations, *J. Phys. Chem. Lett.* 8 (2017) 1449–1457. doi:10.1021/acs.jpcllett.7b00255.
- [18] J. C. Slater, Atomic shielding constants, *Phys. Rev.* 36 (1930) 57–64. doi:10.1103/PhysRev.36.57.
- [19] G. te Velde, F. M. Bickelhaupt, E. J. Baerends, C. F. Guerra, S. J. A. van Gisbergen, J. G. Snijders, T. Ziegler, *Chemistry with ADF*, *J. Comput. Chem.* 22 (9) (2001) 931–967. doi:10.1002/jcc.1056.
- [20] E. van Lenthe, E. J. Baerends, Optimized Slater-type basis sets for the elements 1-118, *J. Comput. Chem.* 24 (9) (2003) 1142–1156. doi:10.1002/jcc.10255.
- [21] F. W. Averill, D. E. Ellis, An efficient numerical multicenter basis set for molecular orbital calculations: Application to FeCl₄, *J. Chem. Phys.* 59 (12) (1973) 6412–6418. doi:10.1063/1.1680020.
- [22] A. Zunger, A. J. Freeman, Self-consistent numerical-basis-set linear-combination-of-atomic-orbitals for the study of solids in the local density formalism, *Phys. Rev. B* 15 (10) (1977) 4716–4737. doi:10.1103/PhysRevB.15.4716.
- [23] B. Delley, D. E. Ellis, Efficient and accurate expansion methods for molecules in local density models, *J. Chem. Phys.* 76 (4) (1982) 1949–1982. doi:10.1063/1.443168.
- [24] O. F. Sankey, D. J. Niklewski, Ab initio multicenter tight-binding model for molecular-dynamics simulations and other applications in covalent systems, *Phys. Rev. B* 40 (6) (1989) 3979–3995. doi:10.1103/PhysRevB.40.3979.
- [25] B. Delley, An all-electron numerical method for solving the local density functional for polyatomic molecules, *J. Chem. Phys.* 92 (1) (1990) 508–517. doi:10.1063/1.458452.
- [26] A. P. Horsfield, Efficient ab initio tight binding, *Phys. Rev. B* 56 (11) (1997) 6594–6602. doi:10.1103/PhysRevB.56.6594.

- [27] K. Koepnik, H. Eschrig, Full-potential nonorthogonal local-orbital minimum-basis band-structure scheme, *Phys. Rev. B* 59 (1999) 1743–1757. doi:10.1103/PhysRevB.59.1743.
- [28] J. M. Soler, E. Artacho, J. D. Gale, A. García, J. Junquera, P. Ordejón, D. Sánchez-Portal, The SIESTA method for ab-initio order-N materials simulation, *J. Phys.: Condens. Matter* 14 (2002) 2745–2779. doi:10.1088/0953-8984/14/11/302.
- [29] T. Ozaki, H. Kino, Efficient projector expansion for the ab initio LCAO method, *Phys. Rev. B* 72 (2005) 045121. doi:10.1103/PhysRevB.72.045121.
- [30] V. Blum, R. Gehrke, F. Hanke, P. Havu, V. Havu, X. Ren, K. Reuter, M. Scheffler, Ab initio molecular simulations with numeric atom-centered orbitals, *Comp. Phys. Comm.* 180 (2009) 2175–2196. doi:doi:10.1016/j.cpc.2009.06.022.
- [31] I. Y. Zhang, X. Ren, P. Rinke, V. Blum, M. Scheffler, Numeric atom-centered-orbital basis sets with valence-correlation consistency from H to Ar, *New. J. Phys.* 15 (2013) 123033. doi:10.1088/1367-2630/15/12/123033.
- [32] J. M. Pérez-Jordá, W. Yang, An algorithm for 3D numerical integration that scales linearly with the size of the molecule, *Chem. Phys. Lett.* 241 (1995) 469–476. doi:10.1016/0009-2614(95)00665-Q.
- [33] R. E. Stratmann, G. E. Scuseria, M. J. Frisch, Achieving linear-scaling in exchange-correlation density functional quadratures, *Chem. Phys. Lett.* 257 (1996) 213–223. doi:10.1016/0009-2614(96)00600-8.
- [34] C. Fonseca Guerra, J. G. Snijders, G. te Velde, E. J. Baerends, Towards an order-N DFT method, *Theor. Chem. Acc.* 99 (6) (1998) 391–403. doi:10.1007/s002140050353.
- [35] G. E. Scuseria, Linear scaling density functional calculations with Gaussian orbitals, *J. Phys. Chem. A* 103 (25) (1999) 4782–4790. doi:10.1021/jp990629s.

- [36] T. Ozaki, H. Kino, J. Yu, M. Han, N. Kobayashi, M. Ohfuti, F. Ishii, T. Ohwaki, User's manual of OpenMX, <http://www.openmx-square.org> (2008).
- [37] V. Havu, V. Blum, P. Havu, M. Scheffler, Efficient $O(N)$ integration for all-electron electronic structure calculation using numeric basis functions, *J. Comput. Phys.* 228 (2009) 8367–8379. doi:10.1016/j.jcp.2009.08.008.
- [38] E. S. Larsen, D. McAllister, Fast matrix multiplies using graphics hardware, in: *SC '01 Proceedings of the 2001 ACM/IEEE conference on Supercomputing*, ACM Press, New York, New York, USA, 2001, p. 55. doi:10.1145/582034.582089.
- [39] K. Moreland, E. Angel, The FFT on a GPU, in: *HWWS '03 Proceedings of the ACM SIGGRAPH/EUROGRAPHICS conference on Graphics hardware*, Eurographics Association, Aire-la-Ville, Switzerland, Switzerland, 2003, pp. 112–119.
- [40] I. S. Ufimtsev, T. J. Martínez, Quantum chemistry on graphical processing units. 1. Strategies for two-electron integral evaluation, *J. Chem. Theory Comput.* 4 (2008) 222–231. doi:10.1021/ct700268q.
- [41] I. S. Ufimtsev, T. J. Martínez, Quantum chemistry on graphical processing units. 2. Direct self-consistent-field implementation, *J. Chem. Theory Comput.* 5 (4) (2009) 1004–1015. doi:10.1021/ct800526s.
- [42] I. S. Ufimtsev, T. J. Martínez, Quantum chemistry on graphical processing units. 2. Direct self-consistent-field implementation, *J. Chem. Theory Comput.* 5 (11) (2009) 3138. doi:10.1021/ct900433g.
- [43] I. S. Ufimtsev, T. J. Martínez, Quantum chemistry on graphical processing units. 3. Analytical energy gradients, geometry optimization, and first principles molecular dynamics, *J. Chem. Theory Comput.* 5 (10) (2009) 2619–2628. doi:10.1021/ct9003004.
- [44] N. Luehr, A. Sisto, T. J. Martínez, Gaussian basis set Hartree-Fock, density functional theory, and beyond on GPUs, in: R. C. Walker, A. W. Götz (Eds.), *Electronic Structure Calculations on Graphics Processing Units: From Quantum Chemistry to Condensed Matter*

Physics, John Wiley & Sons, Ltd., West Sussex, United Kingdom, 2016, Ch. 4, pp. 67–100.

- [45] K. Yasuda, Two-electron integral evaluation on the graphics processor unit, *J. Comput. Chem* 29 (2007) 334–342. doi:10.1002/jcc.20779.
- [46] K. Yasuda, Accelerating density functional calculations with graphics processing unit, *J. Chem. Theory Comput.* 4 (8) (2008) 1230–1236. doi:10.1021/ct8001046.
- [47] X. Gonze, F. Jollet, F. Abreu Araujo, D. Adams, B. Amadon, T. Applencourt, C. Audouze, J.-M. Beuken, J. Bieder, A. Bokhanchuk, E. Bousquet, F. Bruneval, D. Caliste, M. Côté, F. Dahm, F. Da Pieve, M. Delaveau, M. Di Gennaro, B. Dorado, C. Espejo, G. Geneste, L. Genovese, A. Gerossier, M. Giantomassi, Y. Gillet, D. R. Hamann, L. He, G. Jomard, J. Laflamme Janssen, S. Le Roux, A. Levitt, A. Lherbier, F. Liu, I. Lukačević, A. Martin, C. Martins, M. J. T. Oliveira, S. Poncé, Y. Pouillon, T. Rangel, G.-M. Rignanese, A. H. Romero, B. Rousseau, O. Rubel, A. A. Shukri, M. Stankovski, M. Torrent, M. J. Van Setten, B. Van Troeye, M. J. Verstraete, D. Waroquiers, J. Wiktor, B. Xu, A. Zhou, J. W. Zwanziger, Recent developments in the ABINIT software package, *Comput. Phys. Commun.* 205 (2016) 106 – 131. doi:10.1016/j.cpc.2016.04.003.
- [48] H. van Schoot, L. Visscher, GPU acceleration for density functional theory with Slater-type orbitals, in: R. C. Walker, A. W. Götz (Eds.), *Electronic Structure Calculations on Graphics Processing Units: From Quantum Chemistry to Condensed Matter Physics*, John Wiley & Sons, Ltd., West Sussex, United Kingdom, 2016, Ch. 5, pp. 101–114.
- [49] L. Genovese, M. Ospici, T. Deutsch, J.-F. Méhaut, A. Neelov, S. Goedecker, Density functional theory calculation on many-cores hybrid central processing unit-graphics processing unit architectures, *J. Chem. Phys* 131 (2009) 034103. doi:10.1063/1.3166140.
- [50] L. Genovese, B. Videau, D. Caliste, J.-F. Méhaut, S. Goedecker, T. Deutsch, Wavelet-based density functional theory on massively parallel hybrid architectures, in: R. C. Walker, A. W. Götz (Eds.), *Electronic Structure Calculations on Graphics Processing Units: From*

Quantum Chemistry to Condensed Matter Physics, John Wiley & Sons, Ltd., West Sussex, United Kingdom, 2016, Ch. 6, pp. 115–134.

- [51] O. Schütt, P. Messmer, J. Hutter, J. VandeVondele, GPU accelerated sparse matrix-matrix multiplication for linear scaling density functional theory, in: R. C. Walker, A. W. Götz (Eds.), *Electronic Structure Calculations on Graphics Processing Units: From Quantum Chemistry to Condensed Matter Physics*, John Wiley & Sons, Ltd., West Sussex, United Kingdom, 2016, Ch. 8, pp. 173–190.
- [52] S. Hakala, V. Havu, J. Enkovaara, R. Nieminen, Parallel electronic structure calculations using multiple graphics processing units (GPUs), in: P. Manninen, P. Öster (Eds.), *Lecture Notes in Computer Science*, Vol. 7782, Springer-Verlag Berlin Heidelberg, 2013, pp. 63–76.
- [53] J. Yan, L. Li, C. O’Grady, Graphics processing unit acceleration of the random phase approximation in the projector augmented wave method, *Comput. Phys. Commun.* 184 (12) (2013) 2728–2733. doi:10.1016/j.cpc.2013.07.014.
- [54] S. Hakala, J. Enkovaara, V. Havu, J. Yan, L. Li, C. O’Grady, R. M. Nieminen, Grid-based projector-augmented wave method, in: R. C. Walker, A. W. Götz (Eds.), *Electronic Structure Calculations on Graphics Processing Units: From Quantum Chemistry to Condensed Matter Physics*, John Wiley & Sons, Ltd., West Sussex, United Kingdom, 2016, Ch. 9, pp. 191–210.
- [55] W. Jia, J. Wang, X. Chi, L.-W. Wang, GPU implementation of the linear scaling three dimensional fragment method for large scale electronic structure calculations, *Comput. Phys. Commun.* 211 (2017) 8–15. doi:10.1016/j.cpc.2016.07.003.
- [56] X. Andrade, J. Alberdi-Rodriguez, D. A. Strubbe, M. J. T. Oliveira, F. Nogueira, A. Castro, J. Muguerza, A. Arruabarrena, S. G. Louie, A. Aspuru-Guzik, A. Rubio, M. A. L. Marques, Time-dependent density-functional theory in massively parallel computer architectures: the OCTOPUS project, *J. Phys.: Condens. Matter* 24 (23) (2012) 233202. doi:10.1088/0953-8984/24/23/233202.

- [57] X. Andrade, A. Aspuru-Guzik, Real-space density functional theory on graphical processing units: Computational approach and comparison to Gaussian basis set methods, *J. Chem. Theory Comput.* 9 (10) (2013) 4360–4373. doi:10.1021/ct400520e.
- [58] X. Andrade, A. Aspuru-Guzik, Application of graphics processing units to accelerate real-space density functional theory and time-dependent density functional theory calculations, in: R. C. Walker, A. W. Götz (Eds.), *Electronic Structure Calculations on Graphics Processing Units: From Quantum Chemistry to Condensed Matter Physics*, John Wiley & Sons, Ltd., West Sussex, United Kingdom, 2016, Ch. 10, pp. 211–237.
- [59] K. Wilkinson, C.-K. Skylaris, Porting ONETEP to graphical processing unit-based coprocessors. 1. FFT box operations, *J. Comput. Chem.* 34 (28) (2013) 2446–2459. doi:10.1002/jcc.23410.
- [60] L. Wang, Y. Wu, W. Jia, W. Gao, X. Chi, L.-W. Wang, Large scale plane wave pseudopotential density functional theory calculations on GPU clusters, in: *SC '11: Proceedings of 2011 International Conference for High Performance Computing, Networking, Storage and Analysis*, ACM, New York, NY, USA, 2011, p. 71. doi:10.1145/2063384.2063479.
- [61] W. Jia, Z. Cao, L. Wang, J. Fu, X. Chi, W. Gao, L.-W. Wang, The analysis of a plane wave pseudopotential density functional theory code on a GPU machine, *Comput. Phys. Commun.* 18 (1) (2013) 9–18. doi:10.1016/j.cpc.2012.08.002.
- [62] W. Jia, J. Fu, Z. Cao, L. Wang, X. Chi, W. Gao, L.-W. Wang, Fast plane wave density functional theory molecular dynamics calculations on multi-GPU machines, *J. Comput. Phys.* 251 (2013) 102–115. doi:10.1016/j.jcp.2013.05.005.
- [63] PWmat, <http://www.pwmatus.com/> (accessed June 12, 2019).
- [64] L. Vogt, R. Olivares-Amaya, S. Kermes, Y. Shao, C. Amador-Bedolla, A. Aspuru-Guzik, Accelerating resolution-of-the-identity second-order Møller-Plesset quantum chemistry calculations with graphical processing units, *J. Phys. Chem. A* 112 (10) (2008) 2049–2057. doi:10.1021/jp0776762.

- [65] R. Olivares-Amaya, M. A. Wilson, R. G. Edgar, L. Vogt, Y. Shao, A. Aspuru-Guzik, Accelerating correlated quantum chemistry calculations using graphical processing units and a mixed precision matrix multiplication library, *J. Chem. Theory Comput.* 6 (1) (2010) 135–144. doi:10.1021/ct900543q.
- [66] F. Spiga, I. Girotto, phiGEMM: a CPU-GPU library for porting Quantum ESPRESSO on hybrid systems, in: *PDP '12 Proceedings of the 2012 20th Euromicro International Conference on Parallel, Distributed and Network-based Processing*, IEEE Computer Society, Washington, DC, USA, 2012, pp. 368–375. doi:10.1109/PDP.2012.72.
- [67] J. Romero, E. Phillips, G. Ruetsch, M. Fatica, F. Spiga, P. Giannozzi, A performance study of Quantum ESPRESSO's PWscf code on multi-core and GPU systems, in: S. Jarvis, S. Wright, S. Hammond (Eds.), *Lecture Notes in Computer Science*, Vol. 10724, Springer International Publishing AG, 2018, pp. 67–87. doi:10.1007/978-3-319-72971-8_4.
- [68] S. Moore, E. Briggs, M. Hodak, W. Lu, J. Bernholc, C.-W. Lee, Scaling the RMG quantum mechanics code, in: *BW-XSEDE '12 Proceedings of the Extreme Scaling Workshop*, University of Illinois at Urbana-Champaign Champaign, IL, USA, 2012.
- [69] RMG - a real space multigrid DFT code, <http://www.rmgdft.org/> (accessed June 12, 2019).
- [70] S. Maintz, B. Eck, R. Dronskowski, Speeding up plane-wave electronic-structure calculations using graphics-processing units, *Comput. Phys. Commun.* 182 (7) (2011) 1421–1427. doi:10.1016/j.cpc.2011.03.010.
- [71] M. Hutchinson, M. Widom, VASP on a GPU: Application to exact-exchange calculations of the stability of elemental boron, *Comput. Phys. Commun.* 183 (7) (2012) 1422–1426. doi:10.1016/j.cpc.2012.02.017.
- [72] M. Hacene, A. Anciaux-Sedrakian, X. Rozanska, D. Klahr, T. Guignon, P. Fleurat-Lessard, Accelerating VASP electronic structure calculations

- using graphic processing units, *J. Comput. Chem* 33 (32) (2012) 2581–2589. doi:10.1002/jcc.23096.
- [73] M. Hutchinson, P. Fleurat-Lessard, A. Anciaux-Sedrakian, D. Stosic, J. Bédorf, S. Tariq, Plane-wave density functional theory, in: R. C. Walker, A. W. Götz (Eds.), *Electronic Structure Calculations on Graphics Processing Units: From Quantum Chemistry to Condensed Matter Physics*, John Wiley & Sons, Ltd., West Sussex, United Kingdom, 2016, Ch. 7, pp. 135–172.
- [74] cuBLAS API Reference Guide, <http://docs.nvidia.com/cuda/cublas> (accessed June 12, 2019).
- [75] cuFFT API Reference Guide, <https://docs.nvidia.com/cuda/cufft/> (accessed June 12, 2019).
- [76] Thrust API Reference Guide, <https://docs.nvidia.com/cuda/thrust/> (accessed June 12, 2019).
- [77] A. Marek, V. Blum, R. Johanni, V. Havu, B. Lang, T. Auckenthaler, A. Heinecke, H.-J. Bungartz, H. Lederer, The ELPA library: scalable parallel eigenvalue solutions for electronic structure theory and computational science, *J. Phys.: Condens. Matter* 26 (2014) 213201. doi:10.1088/0953-8984/26/21/213201.
- [78] P. Kûs, A. Marek, H. Lederer, GPU optimization of large-scale eigenvalue solver, in: F. A. Radu, K. Kumar, I. Berre, J. M. Nordbotten, I. S. Pop (Eds.), *Lecture Notes in Computational Science and Engineering*, Vol. 126, Springer Nature Switzerland AG, 2019, Ch. 9, pp. 123–131. doi:10.1007/978-3-319-96415-7\9.
- [79] P. Kûs, A. Marek, S. S. Köcher, H.-H. Kowalski, C. Carbogno, C. Scheurer, K. Reuter, M. Scheffler, H. Lederer, Optimizations of the eigensolvers in the ELPA library, *Parallel Comput.* 85 (2019) 167–177. doi:10.1016/j.parco.2019.04.003.
- [80] S. Tomov, J. Dongarra, M. Baboulin, Towards dense linear algebra for hybrid GPU accelerated manycore systems, *Parallel Comput.* 36 (2010) 232–240. doi:10.1016/j.parco.2009.12.005.

- [81] S. Tomov, R. Nath, H. Ltaief, J. Dongarra, Dense linear algebra solvers for multicore with GPU accelerators, in: 2010 IEEE International Symposium on Parallel & Distributed Processing, Workshops and Phd Forum (IPDPSW), IEEE Computer Society, 2010, pp. 1–8. doi:10.1109/IPDPSW.2010.5470941.
- [82] J. Dongarra, M. Gates, A. Haidar, J. Kurzak, P. Luszczek, S. Tomov, I. Yamazaki, Accelerating numerical dense linear algebra calculations with GPUs, in: V. Kindratenko (Ed.), Numerical Computations with GPUs, Springer International Publishing Switzerland, 2014, Ch. 1, pp. 3–28. doi:10.1007/978-3-319-06548-9_1.
- [83] F. Knuth, C. Carbogno, V. Atalla, V. Blum, M. Scheffler, All-electron formalism for total energy strain derivatives and stress tensor components for numeric atom-centered orbitals, *Comput. Phys. Commun.* 190 (2015) 33–50. doi:10.1016/j.cpc.2015.01.003.
- [84] L. Nemeč, V. Blum, P. Rinke, M. Scheffler, Thermodynamic equilibrium conditions of graphene films on SiC, *Phys. Rev. Lett.* 111 (2013) 065502. doi:10.1103/PhysRevLett.111.065502.
- [85] S. V. Levchenko, X. Ren, J. Wieferink, R. Johanni, P. Rinke, V. Blum, M. Scheffler, Hybrid functionals for large periodic systems in an all-electron, numeric atom-centered basis framework, *Comput. Phys. Comm.* 192 (2015) 60–69. doi:10.1016/j.cpc.2015.02.021.
- [86] V. W.-Z. Yu, F. Corsetti, A. García, W. P. Huhn, M. Jacquelin, W. Jia, B. Lange, J. Lu, W. Mi, A. Seifitokaldani, Á. Vázquez-Mayagoitia, C. Yang, H. Yang, V. Blum, ELSI: A unified software interface for Kohn-Sham electronic structure solvers, *Comput. Phys. Commun.* 222 (2018) 267–285. doi:10.1016/j.cpc.2017.09.007.
- [87] K. Lejaeghere, G. Bihlmayer, T. Björkman, P. Blaha, S. Blügel, V. Blum, D. Caliste, I. E. Castelli, S. J. Clark, A. Dal Corso, et al., Reproducibility in density functional theory calculations of solids, *Science* 351 (6280) (2016) aad3000. doi:10.1126/science.aad3000.
- [88] X. Ren, P. Rinke, V. Blum, J. Wieferink, A. Tkatchenko, A. Sanfilippo, K. Reuter, M. Scheffler, Resolution-of-identity approach to

- Hartree-Fock, hybrid density functionals, RPA, MP2 and GW with numeric atom-centered orbital basis functions, *New J. of Phys.* 14 (2012) 053020. doi:10.1088/1367-2630/14/5/053020.
- [89] A. C. Ihrig, J. Wieferink, I. Y. Zhang, M. Ropo, X. Ren, P. Rinke, M. Scheffler, V. Blum, Accurate localized resolution of identity approach for linear-scaling hybrid density functionals and for many-body perturbation theory, *New J. of Phys.* 17 (9) (2015) 093020. doi:10.1088/1367-2630/17/9/093020.
- [90] M. J. van Setten, F. Caruso, S. Sharifzadeh, X. Ren, M. Scheffler, F. Liu, J. Lischner, L. Lin, J. R. Deslippe, S. G. Louie, C. Yang, F. Weigend, J. B. Neaton, F. Evers, P. Rinke, GW100: Benchmarking G0W0 for molecular systems, *J. Chem. Theory Comput.* 11 (12) (2015) 5665–5687. doi:10.1021/acs.jctc.5b00453.
- [91] W. P. Huhn, V. Blum, One-hundred-three compound band-structure benchmark of post-self-consistent spin-orbit coupling treatments in density functional theory, *Phys. Rev. Mater.* 1 (2017) 033803. doi:10.1103/PhysRevMaterials.1.033803.
- [92] T. Auckenthaler, V. Blum, H.-J. Bungartz, T. Huckle, R. Johanni, L. Krämer, B. Lang, H. Lederer, P. Willems, Parallel solution of partial symmetric eigenvalue problems from electronic structure calculations, *Parallel Comput.* 37 (2011) 783–794. doi:10.1016/j.parco.2011.05.002.
- [93] S. Goedecker, Linear scaling electronic structure methods, *Rev. Mod. Phys.* 71 (4) (1999) 1085–1123. doi:10.1103/RevModPhys.71.1085.
- [94] D. R. Bowler, T. Miyazaki, O(N) methods in electronic structure calculations, *Reports on Progress in Physics* 75 (3) (2012) 036503. doi:10.1088/0034-4885/75/3/036503.
- [95] L. Lin, M. Chen, C. Yang, L. He, Accelerating atomic orbital-based electronic structure calculation via pole expansion and selected inversion, *Journal of Physics: Condensed Matter* 25 (29) (2013) 295501. doi:10.1088/0953-8984/25/29/295501.
- [96] V. I. Lebedev, Values of the nodes and weights of quadrature formulas of Gauss-Markov type for a sphere from the ninth to seventeenth order

of accuracy that are invariant with respect to an octahedron group with inversion, *Zh. Vychisl. Mat. Mat. Fiz.* 15 (1) (1975) 48–54. doi:10.1016/0041-5553(75)90133-0.

- [97] V. I. Lebedev, Quadratures on a sphere, *Zh. Vychisl. Mat. Mat. Fiz.* 16 (2) (1976) 293–306. doi:10.1016/0041-5553(76)90100-2.
- [98] V. I. Lebedev, D. N. Laikov, A quadrature formula for the sphere of the 131st algebraic order of accuracy, *Dokl. Math.* 59 (1999) 477–481.
- [99] B. Delley, High order integration schemes on the unit sphere, *J. Comput. Chem.* 17 (9) (1996) 1152–1155.
- [100] A. D. Becke, A multicenter numerical integration scheme for polyatomic molecules, *J. Chem. Phys.* 88 (4) (1988) 2547–2553. doi:10.1063/1.454033.
- [101] J. P. Perdew, K. Burke, M. Ernzerhof, Generalized Gradient Approximation made simple, *Phys. Rev. Lett.* 77 (18) (1996) 3865–3868. doi:10.1103/PhysRevLett.77.3865.
- [102] B. Delley, Fast calculation of electrostatics in crystals and large molecules, *J. Phys. Chem.* 100 (15) (1996) 6107–6110. doi:10.1021/jp952713n.